CANCER

Mutant p53 protects triple-negative breast adenocarcinomas from ferroptosis in vivo

Denada Dibra[1], Shunbin Xiong[1], Sydney M. Moyer[1,2], Adel K. El-Naggar[3], Yuan Qi[4], Xiaoping Su[4], Elisabeth K. Kong[4], Anil Korkut[4], Guillermina Lozano[1,2]*

The *TP53* tumor suppressor gene is mutated early in most of the patients with triple-negative breast cancer (TNBC). The most frequent *TP53* alterations are missense mutations that contribute to tumor aggressiveness. Here, we used an autochthonous somatic TNBC mouse model, in which mutant p53 can be toggled on and off genetically while leaving the tumor microenvironment intact and wild-type for p53 to identify physiological dependencies on mutant p53. In TNBCs that develop in this model, deletion of two different hotspot p53R172H and p53R245W mutants triggers ferroptosis in vivo, a cell death mechanism involving iron-dependent lipid peroxidation. Mutant p53 protects cells from ferroptosis inducers, and ferroptosis inhibitors reverse the effects of mutant p53 loss in vivo. Single-cell transcriptomic data revealed that mutant p53 protects cells from undergoing ferroptosis through NRF2-dependent regulation of *Mgst3* and *Prdx6*, which encode two glutathione-dependent peroxidases that detoxify lipid peroxides. Thus, mutant p53 protects TNBCs from ferroptotic death.

INTRODUCTION

Tumor-specific alterations dictate tumor dependencies and present potential vulnerabilities (*1*). The *TP53* tumor suppressor gene is deleted or mutated in 84% of triple-negative/basal-like breast cancers and 75% of *HER2*-amplified breast cancers, suggesting that *TP53* alterations are drivers of breast cancer (*2*). The most frequent *TP53* alterations are missense mutations that occur in the DNA binding domain, which result in mutant proteins that lack transcriptional activity. In addition, many p53 missense mutants have gain-of-function (GOF) properties that affect mobility and invasiveness, eventually leading to metastasis (*3–7*). Studies from our group and others have indicated that mutant p53 protein stability is needed for these GOF activities (*5, 6, 8–10*). Often, GOF activities of mutant p53 are observed in vivo but not in vitro, indicating context matters in deciphering the physiological functions of mutant p53 (*11, 12*).

The physiological role of hotspot mutant p53 in tumor maintenance in vivo is understudied. The deletion of mutant p53 in autochthonous lymphomas and colon adenocarcinomas in vivo reduces tumor growth (*13, 14*). The mechanism by which lymphomas regress is unknown; while deletion of mutant p53 in colorectal cancers results in a signal transducers and activators of transcription 3 (Stat3)–mediated inhibition of tumor growth and invasion (*14*). However, in these studies, mutant p53 is expressed in all cells, and deletion of mutant *Trp53* occurs in tumor cells and cells in the tumor microenvironment (TME), muddling interpretation of these results.

In breast cancers, the physiological relevance of mutant p53 is also understudied. We recently developed an autochthonous somatic K14-Cre–driven triple-negative breast cancer (TNBC) mouse model with p53R172H and p53R245W mutations (corresponding to p53R175H and p53R248W hotspots in patients) in which mutant

Trp53 can be toggled on and off genetically only in tumor cells while leaving the TME intact and wild type for p53 (*15*). p53R172H and p53R245W drive development of TNBC with a median latency of 1 year. Most breast tumors are adenocarcinomas (*15*). To delete mutant *Trp53* in these TNBCs, we used CRISPR-Cas9. These breast tumors express Cas9 from the *Rosa26*[LSL CAS9-P2A-EGFP/+] locus only in tumor cells but not in the TME. Tumors were injected with adeno-associated virus (AAV) viral particles expressing two single-guide RNAs (sgRNAs) in a single vector that target p53 exons 2 and 7 (AAV-Δmut-p53) or AAV expressing two nontargeting sgRNAs (AAV-Control). Deletion of either mutant blunts tumor growth, causes cell death independent of apoptosis, and extends survival of mice, indicating potential vulnerabilities for mutant-p53 breast cancer patients for future therapies. Downstream analyses revealed that deletion of mutant *Trp53* activated the cGAS-STING pathway, indicating cell extrinsic effects, but did not cause apoptosis implicating other mechanisms of tumor regression. Thus, we were poised to mechanistically examine dependencies on mutant p53 in these TNBCs. By using single-cell transcriptomics, we found that mutant p53 mitigates oxidative stress and protects cells against ferroptosis, a cell death mechanism involving iron-dependent lipid peroxidation, through the NFE2 like bZIP transcription factor 2 (NRF2)–dependent regulation of *Mgst3* and *Prdx6*, which encode two glutathione-dependent peroxidases that detoxify lipid peroxides.

RESULTS

Mutant p53 protects breast adenocarcinomas from ferroptosis in vivo

We generated two somatic and spontaneous breast cancer mouse models with mutant p53R172H or p53R245W expression driven specifically by *K14-Cre* in epithelial cells (*Trp53*[wm-R172H/fl], *K14-Cre* and *Rosa26*[LSL C][AS9-P2A-EGFP/+] alleles, abbreviated P[172]CC, and *Trp53*[wm-R245W/fl], *K14-Cre* and *Rosa26*[LSL C][AS9-P2A-EGFP/+] alleles, abbreviated P[245]CC) (*15*). These mice express mutant p53 (and no wild-type p53) and Cas9 specifically in epithelial cells and develop breast adenocarcinomas and sarcomas, which are negative for *Esr1*, *Pgr*, and *Erbb2*. The targeted deletion of mutant *Trp53* using

[1]Department of Genetics, The University of Texas MD Anderson Cancer Center, Houston, TX 77030, USA. [2]Genetics and Epigenetics Program, The University of Texas MD Anderson Cancer Center UTHealth Graduate School of Biomedical Sciences, Houston, TX 77030, USA. [3]Department of Pathology, The University of Texas MD Anderson Cancer Center, Houston, TX 77030, USA. [4]Department of Bioinformatics and Computational Biology, The University of Texas MD Anderson Cancer Center, Houston, TX 77030, USA.
*Corresponding author. Email: gglozano@mdanderson.org

AAV-sgRNA to *Trp53* in approximately 35% of cancer cells causes tumor regression in 50% of mice 3 days after the removal of mutant *Trp53* (*15*). Mutant *Trp53* deletion also delays tumor growth and extends survival of mice, indicating dependence on mutant p53 for tumor growth (fig. S1, A and B) (*15*).

To elucidate the mechanism(s) underlying dependence on mutant p53, we analyzed breast adenocarcinomas from $P^{172}CC$ mice treated with either AAV-Control (*n* = 3) or AAV-Δmut-p53 (*n* = 3) acutely within 8 days after last AAV treatment. Histological analyses performed shortly after deletion of mutant *Trp53* showed extensive lesions of ballooned epithelial cells with lipid droplet–like structures (Fig. 1A). All three tumors examined within this time frame had massive lipid-like structures. This phenotype is reminiscent of cells undergoing ferroptosis, a unique form of cell death linked to reactive oxygen species (ROS) accumulation, lipid peroxidation, and the metabolic disruption of iron homeostasis (fig. S1C). We further assessed these lesions for the accumulation of 4-hydroxynonenal (4HNE), a by-product of lipid peroxidation, at various time points and found that two of the three tumors analyzed (the ones harvested 2 and 4 days after the last AAV-Δmut-p53 injection) were positive for 4HNE after mutant *Trp53* deletion (Fig. 1A). AAV-Control–treated tumors were negative for 4HNE staining. Red Oil O staining of three tumors also showed lipid accumulation (Fig. 1B).

Next, we analyzed adenocarcinomas from $P^{245}CC$ mice treated with either AAV-Control (*n* = 5) or AAV-Δmut-p53 (*n* = 8) acutely after mutant *Trp53* deletion (3 days after second injection). Here, we also observed extensive lesions of ballooned epithelial cells with lipid droplet–like structures shortly after deletion of mutant *Trp53* (Fig. 1C). Eighty seven percent of tumors examined 3 days after the second AAV-Δmut-p53 treatment had massive lipid-like structures. We also assessed these lesions for accumulation of 4HNE 3 days after the second injection and found that 50% of mice (4/8) were positive for 4HNE after mutant *Trp53R245W* deletion (Fig. 1C). AAV-Control–treated tumors (*n* = 5) were negative for 4HNE staining. Red Oil O staining from three tumors confirmed lipid accumulation in these droplet-like structures (Fig. 1D). These data suggest that TNBCs from $P^{172}CC$ and $P^{245}CC$ mice undergo ferroptosis in vivo upon loss of mutant *Trp53*.

To determine the human relevance of our findings, analysis of The Cancer Genome Atlas (TCGA) data showed that breast cancers with missense mutant p53, as compared to p53 truncation, were enriched in glutathione metabolism and oxidoreductase activity involving nicotinamide adenine dinucleotide (NAD)/NAD phosphate (NADP) implicating glutathione peroxidase 4 (GPX4) (Fig. 1E). GPX4 detoxifies lipids at the expense of glutathione and reduced form of $NADP^+$. Thus, both murine and patient data indicate that p53 missense mutants regulate tumor sensitivity to ferroptosis.

To test if inhibition of ferroptosis rescued the effects of mutant p53 dependence in vivo, autochthonous tumors from three mice (one $P^{172}CC$ and two $P^{245}CC$) were treated with AAV-Δmut-p53 (following established regimen; fig. S1A) and the ferroptosis inhibitor liproxstatin-1 (given daily starting on the first day of AAV injection; Fig. 1F). Liproxstatin-1 is a radical trapping antioxidant and inhibitor of ferroptosis used both in vitro and in vivo to test for ferroptotic events (*16, 17*). Adenocarcinomas treated with AAV-Δmut-p53 regressed compared to AAV-control treated tumors as previously reported (Fig. 1F, left) (*15*). Tumors treated with AAV-Δmut-p53 and liproxstatin-1 grew substantially better than those treated with AAV-Δmut-p53 alone (Fig. 1F, left). At end point, AAV-Δmut-p53

tumors treated with liproxstatin-1 grew twice as fast as those treated with AAV-Δmut-p53 alone ($P^{172}CC$ and $P^{245}CC$; Fig. 1F, right). Thus, in vivo experiments indicate that deletion of mutant p53 sensitizes cells and tumors to ferroptosis, which is reversed by treatment with liproxistatin-1, an inhibitor of ferroptosis.

Previously, we showed that *Trp53* deletion in vivo elevated pSTING Ser^{366} in breast tumors of $P^{172}CC$ and $P^{245}CC$ genotype, indicative of cGAS-STING pathway activation (*15*). We therefore tested whether inhibition of cGAS-STING pathway by mutant p53 was dependent on inhibition of ferroptosis. We examined pSTING Ser^{366} levels in tumors following mutant *Trp53* deletion in the presence or absence of liproxstatin-1 and observed elevated pSTING Ser^{366} levels regardless of the presence or absence of liproxstatin-1, indicating that mutant p53 regulates cGAS-STING pathway independent of ferroptosis (fig. S1D).

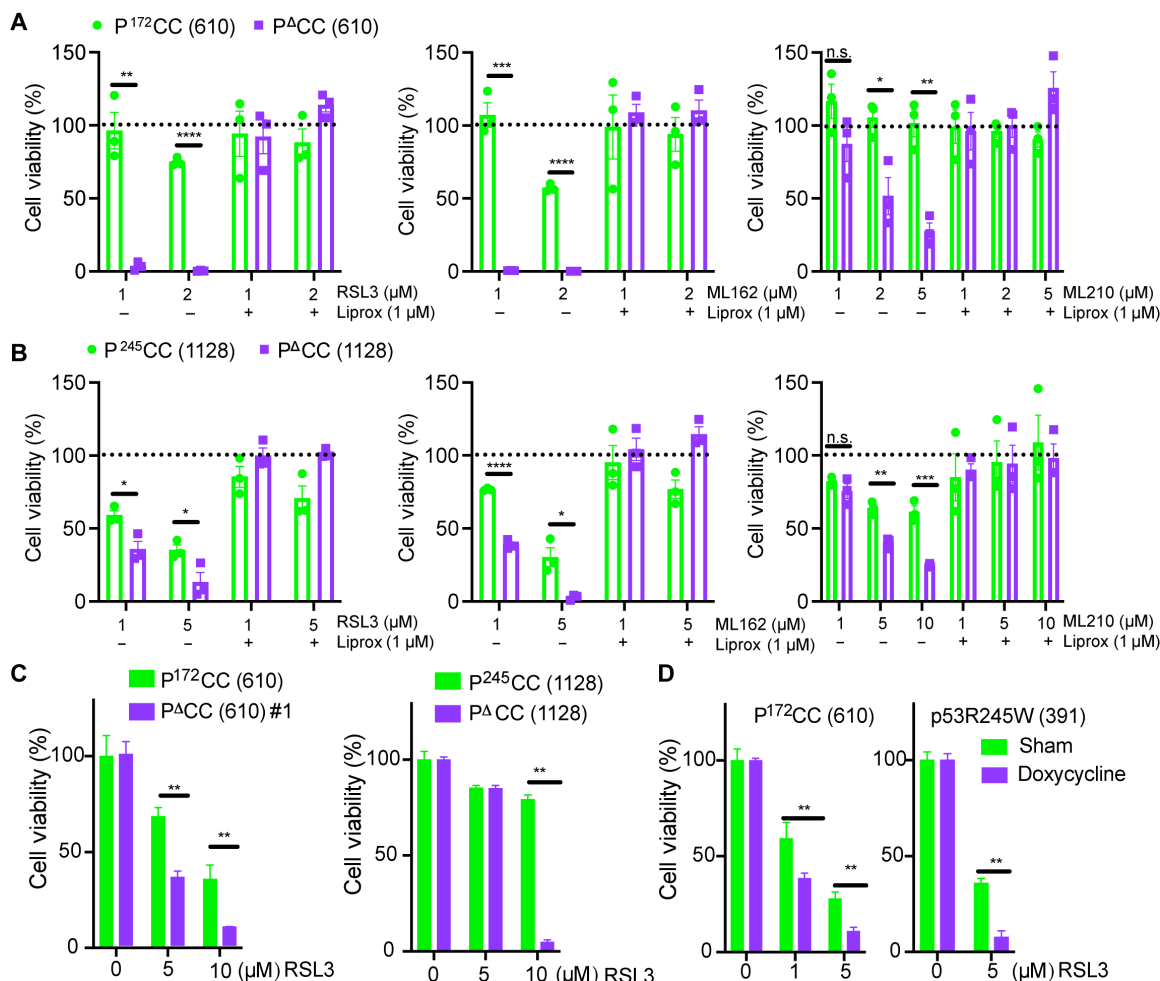## Mutant p53 protects breast adenocarcinomas from ferroptosis at GPX4 level

To validate these in vivo findings, we established cell lines from untreated breast tumors from $P^{172}CC$ mice ($P^{172}CC$ [610] cells) and $P^{245}CC$ mice ($P^{245}CC$ [1128] cells). We then used CRISPR to delete mutant *Trp53* in cell lines and used Western blots to validate loss of p53 (fig. S2A). The clones with mutant *Trp53* deletion ($P^{\Delta}CC$ [610] cells and $P^{\Delta}CC$ [1128] cells) were very sensitive to trypsinization, low cell density seeding, and increased acidity in the media requiring frequent changes of media.

To directly assess the role of mutant p53 in ferroptosis, we treated $P^{172}CC$ [610] cells and its respective mutant p53-deficient clone ($P^{\Delta}CC$ [610]) with RSL3 [(1S,3R)-RSL3], which induces of ferroptosis by inhibiting GPX4 (fig. S1C) (*18*). Mutant p53-deficient cells were more sensitive to RSL3-mediated cell death when compared to mutant p53 proficient ones (Fig. 2A, left). Liproxstatin-1 completely reversed RSL3-mediated cell death, indicating that the cells lacking mutant p53 indeed underwent ferroptosis upon RSL3 treatment (Fig. 2A, left). Similarly, the mutant p53–deficient $P^{\Delta}CC$ [610] cells were sensitive to two other inhibitors of GPX4 (ML162 and ML210) when compared to mutant p53 proficient ones (Fig. 2A, middle and right panels) (*18*). Liproxstatin-1 also reversed ML162- and ML210-mediated cell death, indicating that cells were undergoing ferroptosis. Next, we tested the sensitivity of $P^{245}CC$ (1128) cells and its respective mutant p53-deficient clone $P^{\Delta}CC$ (1128) to RSL3. Similarly, mutant p53R245W-deficient cells were more sensitive to RSL3-mediated cell death when compared to mutant p53 proficient ones (Fig. 2B, left). Liproxstatin-1 again reversed RSL3-mediated cell death (Fig. 2B, left). Comparably, the mutant p53R245W-deficient cells were sensitive to two other inhibitors of GPX4 (ML162 and ML210) when compared to mutant p53 proficient ones (Fig. 2B), and liproxstatin-1 completely reversed cell death. Even at high cell density when cells tend to be resistant to ferroptosis, mutant p53-deficient cells [both $P^{172}CC$ (610) and $P^{245}CC$ mice (1128)] cells remained sensitive to RSL3-mediated cell death when compared to mutant p53-proficient cells (Fig. 2C).

Next, to assess the role of mutant p53 acutely after mutant *Trp53* deletion, $P^{172}CC$ and $P^{245}CC$ cells were infected with a doxycycline-inducible lentiviral vector expressing a sgRNA targeting mutant p53 (*19*). Doxycycline-treated cells were notably more susceptible to ferroptosis than sham-treated cells (Fig. 2D and fig. S2C). Thus, multiple lines of evidence suggest that mutant p53 protects cells from ferroptosis through GPX4 because mutant p53-deficient clones were sensitive to RSL3, ML210, and ML162 but not erastin (an inhibitor of
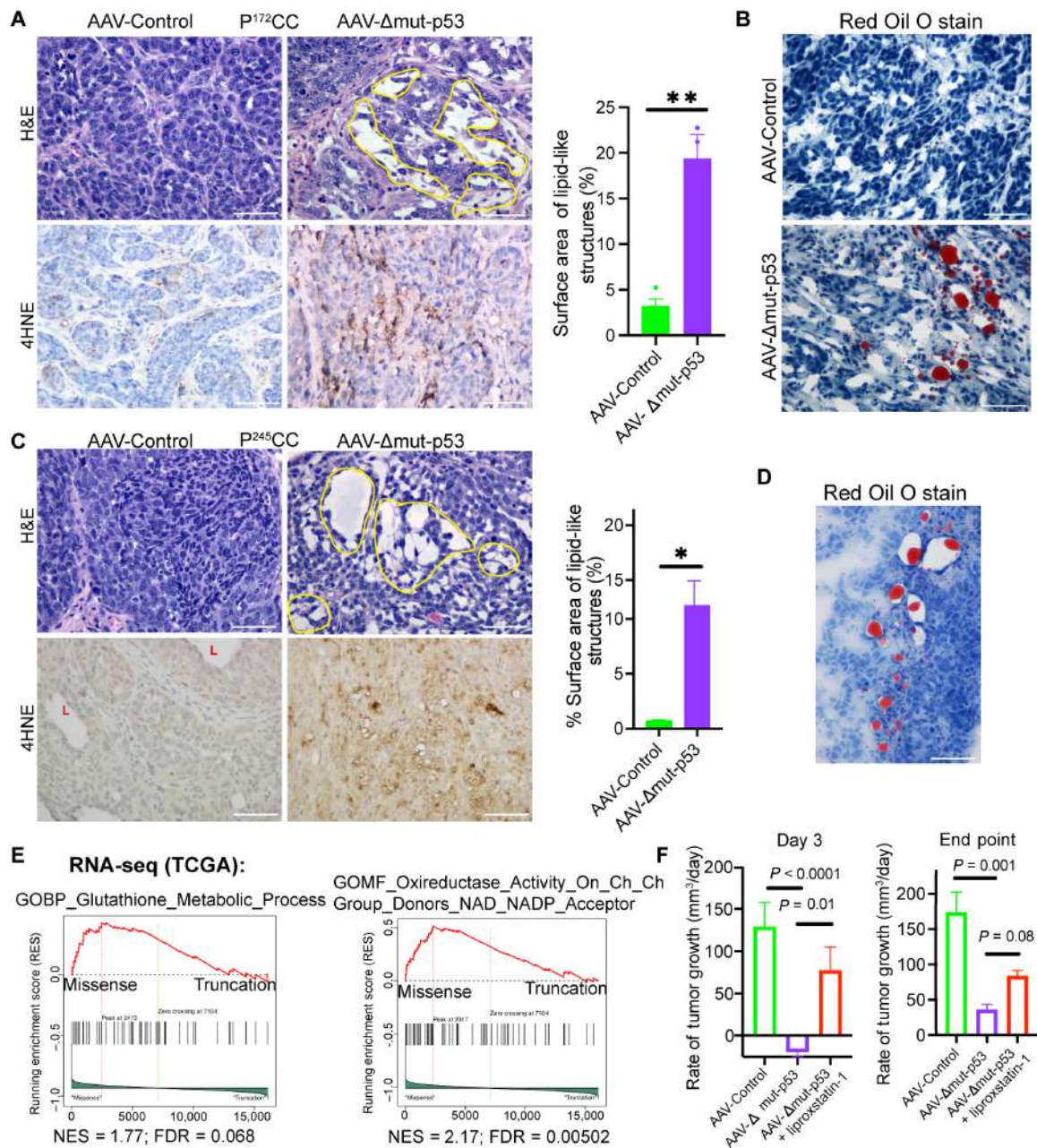
Fig. 1. Mutant p53 protects breast adenocarcinomas from ferroptosis in vivo. (**A**) Representative hematoxylin and eosin (H&E)– and 4HNE-stained sections of P^{172}CC adenocarcinomas treated with AAV-Control (left) or AAV-Δmut-p53 (right) and quantification of lipid droplets in three fields of view per sample from AAV-Control ($n = 3$) 5, and 12 days after last AAV injection or AAV-Δmut-p53 ($n = 3$) 2, 4, and 8 days after last AAV injection. Yellow outline, lipid droplets. H&E shown is from a tumor harvested on day 8 after last AAV injection. Image for the 4HNE is a tumor harvested on day 2 after last AAV injection. Scale bars, 500 μm. (**B**) Red Oil O staining of a tumor treated with AAV-Control and AAV-Δmut-p53 (P^{172}CC mice). Image is from tumor harvested on day 2 after last AAV injection. (**C**) Representative H&E- and 4HNE-stained sections of P^{245}CC adenocarcinomas treated with AAV-Control (left) or AAV-Δmut-p53 (right) and quantification of lipid droplets within the tumor section in three fields of view per sample from AAV-Control ($n = 5$) or AAV-Δmut-p53 ($n = 8$) at 3 days after second treatment. L, lumen of malignant epithelium; yellow outline, lipid droplets. Scale bars, 500 μm. (**D**) Red Oil O staining of a tumor treated with AAV-Δmut-p53 (P^{245}CC mice). (**E**) Gene set enrichment analysis (GSEA) of glutathione metabolic processes and oxidoreductase activity on Ch_CH donors and NAD_NADP acceptors in breast cancer patients with *TP53* missense mutations ($n = 214$) as compared with patients with *TP53* ($n = 110$) truncating mutations. (**F**) Tumor growth rates (mm^3/day) at day 3 (left) or end point (right) for adenocarcinomas from P^{172}CC ($n = 12$) and P^{245}CC ($n = 6$) adenocarcinomas treated with AAV-Control ($n = 5$), AAV-Δmut-p53 ($n = 10$), or AAV-Δmut-p53 plus liproxstatin-1 ($n = 3$). Data are means ± SEM. Significant differences were evaluated by Student's *t* test [(A) and (C)] and one-way analysis of variance (ANOVA) (F). *$P < 0.05$ and **$P < 0.01$. TCGA, The Cancer Genome Atlas. RNA-seq, RNA sequencing; NES, normalized enrichment score; FDR, false discovery rate.

Fig. 2. Mutant p53 protects breast adenocarcinomas from ferroptosis through GPX4. (**A**) Viability of $P^{172}CC$ (610) and its corresponding p53-deleted clone ($P^{\Delta}CC$) treated with ferroptosis inducers RSL3, ML162, ML210, and ferroptosis inhibitor liproxstatin-1 at the indicated concentrations. Liproxstatin-1 was added 30 min before RSL3, ML162, or ML210. Viability was assessed 24 hours after treatment. Dotted line denotes viability of cells treated with sham dimethyl sulfoxide (DMSO). (**B**) Viability of $P^{245}CC$ (1128) and its corresponding p53-deleted clone ($P^{\Delta}CC$) treated with RSL3, ML162, ML210, and liproxstatin-1 at the indicated concentrations. Liproxstatin-1 was added 30 min before treatment with RSL3, ML162, or ML210. Viability was assessed 24 hours after treatment. Dotted line denotes viability of cells treated with sham DMSO. (**C**) Viability of $P^{172}CC$ (left) and $P^{245}CC$ (right) cell lines and their corresponding p53-knockout clones ($P^{\Delta}CC$) treated with RSL3 or sham at high confluency (1×10^4 cells per well). Viability was assessed 24 hours after treatment. (**D**) Viability of $P^{172}CC$ (610, left) and p53R245W germline breast tumor cells (391, right) infected with a doxycycline-inducible lentivirus expressing sgRNAs targeting *Trp53* and treated with sham or doxycycline (1 µg/ml) for 48 hours and subsequently treated with RSL3 for 24 hours. Significant differences between groups were evaluated by Student's *t* test for (A) to (D) *$P < 0.5$, **$P < 0.01$, ***$P < 0.001$, and ****$P < 0.0001$; n.s., not significant.

system X_c^-, SLC7A11; fig. S2D). These findings were specific to adenocarcinoma cell lines but not to a sarcoma cell line developed from the same model (fig. S2E), although both tumor types are equally responsive to mutant *Trp53* deletion in vivo (*15*). Thus, in vitro and in vivo experiments indicate that deletion of mutant *Trp53* sensitizes cells and tumors to ferroptosis, which is reversed by treatment with liproxstatin-1, an inhibitor of ferroptosis.

Single-cell analyses of tumor response to mutant p53 depletion

To elucidate the mechanism(s) underlying mutant p53–dependent regulation of ferroptosis, we performed single-cell RNA sequencing (scRNA-seq) of adenocarcinomas from the $P^{245}CC$ cohort 3 days after the second treatment (Fig. 3A, samples marked in asterisk), with AAV-Control ($N = 2$) or AAV-Δmut-p53 ($N = 5$, fig. S3A). At

this time point, tumors had begun to regress and were positive for ferroptosis markers (see Fig. 1C). Uniform manifold approximation and projection (UMAP) of labeled cell populations identified 22 clusters (Fig. 3B). To unbiasedly characterize the cell type in each cluster, we analyzed the top significantly enriched genes per cluster using gene set enrichment analysis (GSEA). This analysis includes a cell-type signature gene set and selected markers defining cell types (fig. S3, B and C, and table S1) (*20*). Clusters 1, 9, 11, and 14 were identified as epithelial cells from the primary tumor (table S1). Expression of epithelial markers, including *Epcam*, *Krt8*, *Krt18*, and *Krt19*, confirmed that these clusters were epithelial cells (Fig. 3C). In clusters 1, 11, and 14, the proportion of cells from AAV-Δmut-p53–injected tumors were lower than those of cells from AAV-Control–injected tumors, signifying that these clusters were composed of cells most sensitive to mutant *Trp53* loss (Fig. 3D). The proportion
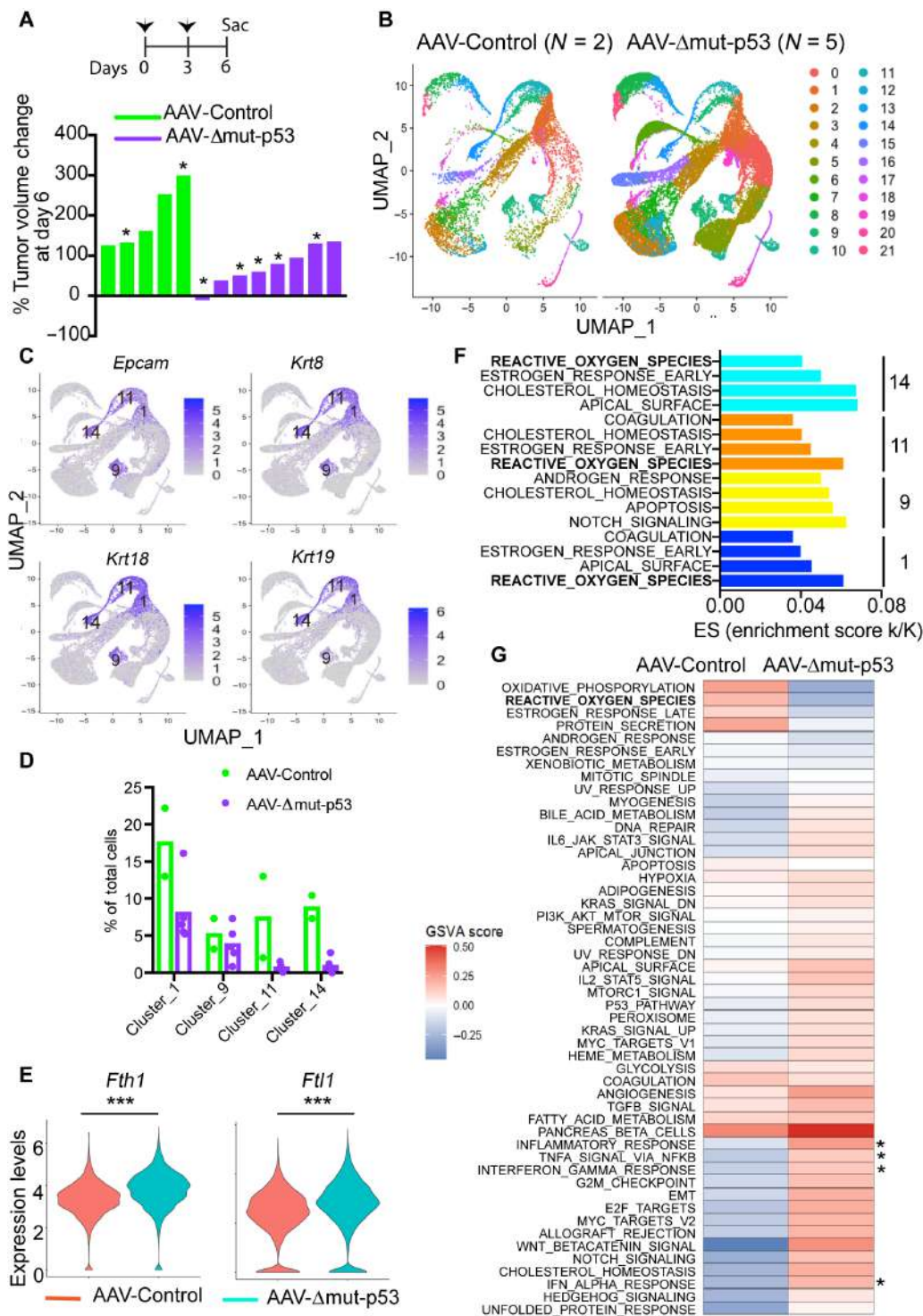
Fig. 3. scRNA-seq analysis of AAV-Δmut-p53 treated TNBCs. (**A**) Top: Treatment regimen; arrows denote the timing of AAV injections. Bottom: Waterfall plot of percent changes in volumes of P[245]CC adenocarcinomas treated with AAV-Control (*n* = 5) or AAV-Δmut-p53 (*n* = 8) at day 6. * denotes samples submitted for scRNA-seq, which contained lipid-like structures and/or were 4HNE positive. (**B**) UMAP of labeled cells pooled and separated by treatment: AAV-Control (*n* = 2) or AAV-Δmut-p53 (*n* = 5) at day 3 after second AAV treatment. (**C**) UMAP of cells expressing selected epithelial markers (*Epcam*, *Krt8*, *Krt18*, and *Krt19*) identified four epithelial clusters. (**D**) Proportions of tumor cells in each of the four clusters by treatment type. Each dot represents one spontaneous tumor. (**E**) Violin plots of *Ftl1* and *Fth1* from the scRNA-seq from epithelial clusters (1, 9, 11, 14) showing the expression levels of genes that are enriched in AAV-Δmut-p53–injected tumors when compared to AAV-Control tumors. ***$P = 1.041 \times 10^{-166}$ (*Fth1*) and ***$P = 1.2755 \times 10^{-60}$ (*Ftl1*). (**F**) Top 4 pathways identified by GSEA in each tumor cell cluster. (**G**) Heatmap of GSVA scores indicating differentially activated pathways in pooled tumor cells grouped by treatment type. * denotes immune-related pathways activated.

of AAV-Δmut-p53 and AAV-Control cells in cluster 9 did not differ significantly (Fig. 3D). Next, we tested whether ferroptosis markers were increased upon mutant *Trp53* deletion in vivo. Existing studies have shown that increased cellular iron levels during ferroptosis induce transcriptional up-regulation of ferritin, a cellular iron storage protein composed of two similar polypeptide chains of ferritin light chain (Ftl1) and ferritin heavy chain (Fth1) (*21*). Upon deletion of mutant *Trp53*, *Ftl1* and *Fth1* levels notably went up in cancer cell clusters 1, 9, 11, and 14 (Fig. 3E).

GSEA identified the ROS and estrogen response pathways as the top pathways in the mutant p53-dependent tumor cell clusters 1, 11, and 14 (Fig. 3F). In addition, the cholesterol pathway was identified in clusters 11 and 14. To better understand mutant p53 dependencies, we used gene set variation analysis (GSVA) (*22*) to identify pathways that were differentially expressed between cancer cells (clusters 1, 9, 11, and 14) with or without mutant *Trp53* deletion. This analysis identified oxidative phosphorylation and ROS pathways as the top pathways enriched in tumors expressing mutant p53 (Fig. 3G). Thus, the ROS pathway emerged in both GSEA and GSVA analyses (Fig. 3, F and G).

Up-regulated immune signaling pathways [interferon-β (IFNβ), tumor necrosis factor, and IFN-γ] were also detected in tumor cells with mutant *Trp53* deletion (Fig. 3F, asterisks), suggesting changes in the TME. Closer inspection of the immune clusters revealed that the number of cells in cluster 8 (γδ T cells) increased upon mutant *Trp53* deletion (fig. S3C). In summary, scRNA-seq data revealed that dependence on mutant p53 encompasses both cell-autonomous (oxidative stress and ROS) and non–cell-autonomous functions (immune pathways).

Mutant p53 regulates *Mgst3* and *Prdx6* to mitigate oxidative stress damage and protect cells against ferroptosis

Ferroptosis is linked to ROS accumulation, lipid peroxidation, and the metabolic disruption of iron homeostasis. Therefore, we tested the hypothesis that mutant p53 protects cancer cells from ferroptosis by disrupting ROS pathway genes. A total of 180 genes were differentially up-regulated [differentially expressed genes (DEGs)] in AAV-Control when compared to AAV-Δmut-p53 tumor clusters (table S2). GSEA analysis of these DEGs showed that tumor cells with mutant *Trp53* ablation were depleted of several antioxidant genes, which mitigate ROS functions, including *Junb*, *Atox1*, *Gclm*, *Prdx2*, *Prdx6*, *Mgst3*, and *Txn1* (Fig. 4A). To determine whether mutant p53 is involved in transcriptionally regulating these genes, we examined their expression in $P^{172}CC$ and $P^{245}CC$ cells and their respective mutant *Trp53*-deleted clones (fig. S2A). *Prdx6* and *Mgst3* transcript levels in $P^{\Delta}CC$ (610, p53R172H) clones #1 and #2 and $P^{\Delta}CC$ (1128, p53R245W) cells were down-regulated 50 to 70% as compared to mutant p53-expressing cells (Fig. 4B, C). The transcript levels of the other ROS transcripts did not differ significantly between groups. *Prdx6* encodes a non-selenium glutathione-dependent peroxidase that completes regeneration of peroxidized cell membranes following an oxidative event (*23*, *24*), and *Mgst3* encodes microsomal glutathione *S*-transferase 3, an enzyme with glutathione-dependent transferase and peroxidase activities (*25*). These two enzymes share many similarities with GPX4, such as their use of glutathione as a cofactor, their peroxidase activity toward lipids, and their ability to inhibit ferroptosis. Previous studies indicate that knockdown of intracellular *Prdx6* in multiple tumor cell lines enhances lipid peroxidation and erastin- or RSL3-induced ferroptosis (*23*, *26–28*).

Therefore, we assessed the roles of these two enzymes on lipid peroxidation, a hallmark of ferroptosis. We used BODIPY C11, a fluorescent probe used to index lipid peroxidation in living cells in tissue culture. BODIPY C11 staining combined with flow cytometric analysis showed that cells with silenced *Mgst3* or *Prdx6* showed a notable increase in lipid peroxidation levels, indicating increased likelihood to undergo ferroptosis (Fig. 4D and fig. S4A).

Next, we assessed the roles of these two enzymes in preventing ferroptosis. Silencing the expression of *Mgst3* or *Prdx6* (fig. S4B) notably decreased survival of p53 mutant cells treated with RSL3 (Fig. 4, E and F). The reverse was also true, as *Mgst3* or *Prdx6* overexpression (fig. S4C) rescued cells with mutant *Trp53* deletion from RSL3-induced death (Fig. 4G). Last, p53R245W overexpression in a mutant p53-deleted cell line ($P^{\Delta}CC$ [610]) desensitized these cells to RSL3-mediated cell death (fig. S4, D and E), while silencing of *Mgst3/Prdx6* in these mutant p53-competent cells resensitized them again to RSL3 (fig. S4F). To test the functional significance of Mgst3 and Prdx6 in vivo, $P^{245}CC$ cells were transfected with short hairpins targeting *Mgst3* or *Prdx6* and injected into the mammary fat pad of nude mice. Knockdown of these genes (Fig. 4H) sensitized tumors to RSL3 treatment (Fig. 4I and fig. S4G). In summary, mutant *Trp53* deletion sensitized breast adenocarcinomas to ferroptosis through two peroxidase enzymes, Mgst3 and Prdx6.

Mutant p53 protects human TNBCs against ferroptosis

To interrogate the translational significance of our findings to human breast cancers, we silenced mutant p53 in six different human breast cancer cell lines with hotspot *TP53* missense mutations. Silencing of mutant *TP53* decreased levels of *MGST3* and *PRDX6* (Fig. 5A) and increased sensitivity to RSL3 in all cell lines tested (Fig. 5B and fig. S5A). Next, we used BODIPY C11 to index lipid peroxidation in living cells in tissue culture. BODIPY C11 staining combined with flow cytometric analysis showed that cells with mutant p53 silencing had an increase in lipid peroxidation (indicating increased likelihood to undergo ferroptosis; fig. S5B). We further tested in vivo the functional significance of our two anti-ferroptotic genes, *MGST3* and *PRDX6*, using MDA-MB-231 cells. Short hairpin knockdown of *MGST3* (~70% reduction) had minimal effects on tumor establishment and growth; meanwhile, complete knockdown of *PRDX6* (~98%) impeded tumor establishment when low (0.5×10^6) or high (3×10^6) number of cancer cells was implanted in vivo (Fig. 5C and fig. S5C).

Similarly, Kaplan-Meier survival analysis showed that the overall survival of breast cancer patients with a high expression of the six antioxidant genes (*ATOX1*, *GCLM*, *PRDX*2, *PRDX6*, *MGST3*, and *TXN*) regulated by mutant p53 (using a threshold of 80%) was significantly worse than that of patients with a low threshold of expression of these genes (using threshold of 20%; Fig. 5D). Thus, analysis of human cell lines and patient data also implicate *MGST3* and *PRDX6* as mutant p53 regulators of ferroptosis.

Mutant p53 mitigates oxidative stress and ferroptosis through the NRF2-dependent regulation of *Mgst3* and *Prdx6*

Missense p53 mutants exhibit gain-of-function activities by interacting with and altering the activities of other transcription factors (e.g., SREBP1/2, ETS2, and VDR) (*4*). We therefore used the ENRICHR-TRRUST database to predict transcription factors that regulate mutant p53-specific ROS pathway genes (from Fig. 4A). The top two predicted transcription factors were PAX5 and NRF2 (Fig. 6A).
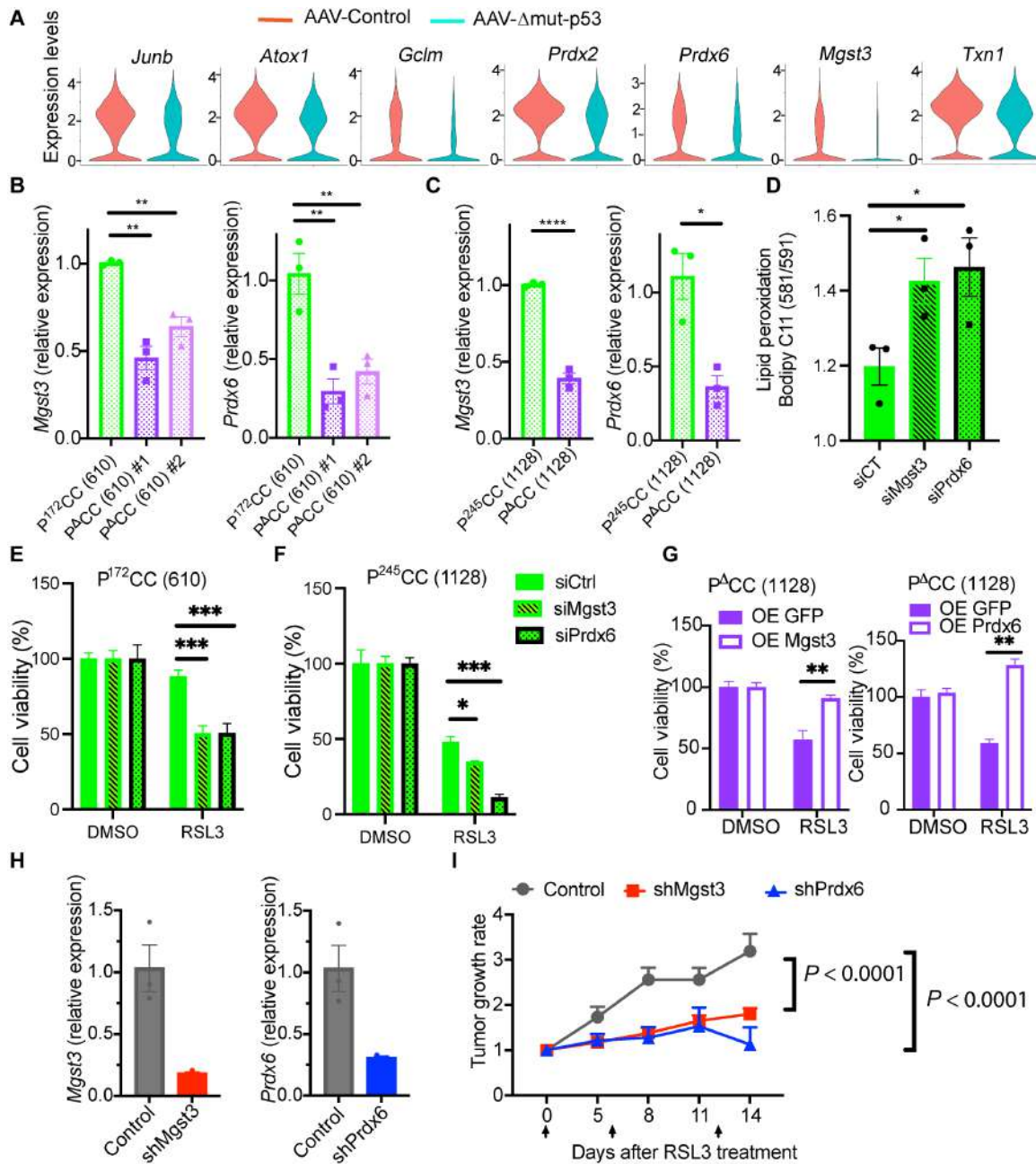
Fig. 4. Mutant p53 mitigates oxidative stress and ferroptosis through regulation of two enzymes, *Mgst3* and *Prdx6*. (**A**) Violin plots of genes from the scRNA-seq associated with the ROS pathway from epithelial clusters (1, 9, 11, 14, from Fig. 3C) showing the expression levels of genes that are enriched in AAV-Control or AAV-Δmut-p53 injected tumors. (**B** and **C**) Reverse transcription quantitative polymerase chain reaction (RT-qPCR) analysis of *Mgst3* and *Prdx6* in P^{172}CC (B) and P^{245}CC (C) cells and their respective *Trp53*-deleted clones. (**D**) Flow cytometric analysis of p53R245W (391) cells with or without *Mgst3* or *Prdx6* silencing at 48 hours and stained with C11-BODIPY, a marker of lipid oxidation. Efficiency of mRNA-mediated silencing is shown in fig. S4A. (**E** and **F**) Viability of P^{172}CC (E) and P^{245}CC (F) cells after siRNA silencing of *Mgst3* or *Prdx6* and treatment with DMSO or RSL3. Viability was assessed 24 hours after treatment. Efficiency of mRNA-mediated silencing shown in fig. S4B. (**G**) Viability of P^{Δ}CC (1128) cells transduced with lentiviral particles overexpressing (OE) cDNAs for *GFP*, *Mgst3*, or *Prdx6* and treated with RSL3 (5 μM). Viability was assessed 24 hours after treatment. Efficiency of lentivirus-mediated overexpression of *Mgst3* and *Prdx6* is shown in S4C. (**H**) Levels or *Mgst3* or *Prdx6* expression in P^{245}CC cells after short hairpin RNA targeting *Mgst3* of *Prdx6*, respectively. (**I**) Tumor growth rates of these cells after injection into nude mice and treatment with RSL3 intratumorally at indicated time points (arrows). Data are means ± SEM. Significant differences between groups was evaluated by one-way ANOVA [(B), (D), and (E)] and Student's *t* test [(C) and (G)] and two-way ANOVA with Dunnett's multiple comparison (I). *$P < 0.5$, **$P < 0.01$, and ****$P < 0.0001$. GFP, green fluorescent protein.
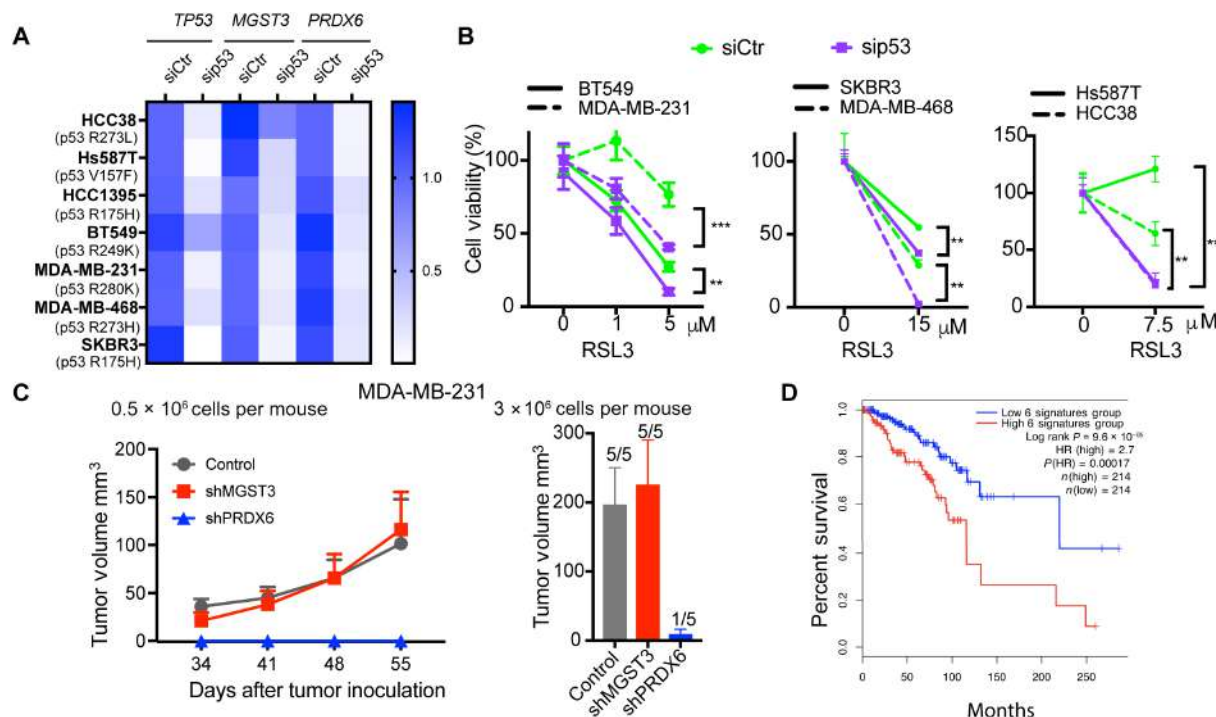
Fig. 5. Mutant p53 protects human TNBCs against ferroptosis. (**A**) RT-qPCR data showing transcript levels of *TP53*, *MGST3*, and *PRDX6* in listed breast tumor cell lines with or without siRNA silencing of mutant *TP53*. p53 mutations for each cell line are listed. (**B**) Viability of human patient breast cancer cells from (A) treated with RSL3. Viability was assessed 24 hours after treatment. (**C**) Tumor growth of MDA-MB-231 cells expressing short hairpin targeting *MGST3* or *PRDX6* in nude animals (*N* = 4 to 5 per group) injected with low (0.5×10^6 at various time points, left) or high (35×10^6 at 42 days, right) cell numbers. (**D**) Kaplan-Meier overall survival curves for breast cancer patients with tumors expressing high levels (80% threshold; 214 patients) or low levels (20% threshold; 214 patients) of our six-gene NRF2 dataset (*ATOX1*, *GCLM*, *PRDX2*, *PRDX6*, *MGST3*, and *TXN*) with a log-rank *P* value of 9.6×10^{-05}. These analyses were done using GEPIA2. Data are means ± SEM. Significant differences between groups was evaluated by Student's *t* test for (A) and (B). *$P < 0.5$, **$P < 0.01$, and ***$P < 0.001$.

PAX5 encodes the B cell lineage–specific activator protein expressed exclusively in B lymphocyte lineage and is unlikely to be mitigating ferroptosis in breast epithelial cells (*29*). NRF2 protects against oxidative and electrophilic stress (*30*). Previously, mutant p53 was shown to regulate proteosome-related gene transcription via an NRF2-dependent mechanism (*31*, *32*). No studies have probed mutant p53/NRF2 interactions in attenuating ferroptosis. NRF2 regulates genes via binding to antioxidant response elements (AREs) (*30*). All but one gene from the identified ROS pathway (*Junb*; Fig. 4A) have ARE binding sites in their promoters. Promoter analysis of 10 kb upstream of the start site of all 180 DEGs enriched in mutant p53 cancer clusters from scRNA-seq analysis showed that 89% of these genes have AREs (Fig. 6B and table S3). Violin plots are shown of top DEGs from cancer clusters (1, 9, 11, 14) regulated by mutant p53 that contain AREs upstream of their promoters and have confirmed NRF2 binding via NRF2–chromatin immunoprecipitation studies by Malhotra *et al.* (*33*) (Fig. 6C). Furthermore, we confirmed that deletion of mutant *Trp53 R245W* also resulted in lower levels of the well-known NRF2 target *Keap1* (fig. S6A).

Brusatol and luteolin are NRF2 inhibitors (*34*, *35*). NRF2 inhibition with either brusatol or luteolin reduced *Mgst3* and *Prdx6* transcripts in both murine and human mutant p53 cells (Fig. 6D and fig. S6, B and C). Furthermore, NRF2 knockdown, phenocopied mutant *Trp53* deletion, and sensitized cells to RSL3 (Fig. 6E and fig. S6D). We next hypothesized that NRF2 and GPX4 inhibition would cooperate to kill mutant p53 cells. Treatment with NRF2 inhibitor

brusatol or the GPX4 inhibitor RSL3 alone killed ~50% of cells with mutant p53, while combined treatment killed these cells efficiently (~98%; Fig. 6F and fig. S6E). We also examined the combined effect of brusatol and RSL3 on cell viability of five human breast cancer cells with p53 missense mutations. In all tested cells, the combination treatment was superior to either treatment alone (Fig. 6G and fig. S6F).

Co-immunoprecipitation experiments with tumor lysates and cell lines showed mutant p53R172H and p53R245W interact with NRF2 (Fig. 6H and fig. S6G). To validate mutant p53 direct interactions with NRF2, we generated cells expressing mutant p53R245W-Flag and NRF2-His tagged proteins. Purified NRF2-His binds p53R245W-Flag bound on FlagM2-beads, indicating direct interaction of mutant p53 to NRF2 (Fig. 6I). Two negative controls, flag-tagged Pla2g16 and p53N15fs, did not interact with NRF2. To test if mutant p53 and NRF2 are located on the same AREs, we used Cleavage Under Targets and Release Using Nuclease (CUT&RUN), a chromatin profiling strategy in which antibody-binding controls cleavage by micrococcal nuclease and releases only antibody-bound protein-DNA complexes. Both mutant p53R245W and NRF2 were present at two ARE sites in the *Prdx6* promoter in P²⁴⁵CC tumor cells but not the respective mutant p53-deleted clone (Fig. 6, J and K).

Published studies indicate that a peptide consisting of human p53 amino acids 98 to 128 binds NRF2 (*32*). Therefore, we generated lentiviral constructs to express full-length murine p53R245W or a truncated version of p53R245W lacking amino acids 98 to 128 and overexpressed these constructs in a P⁻/⁻CC tumor cell line (1374)
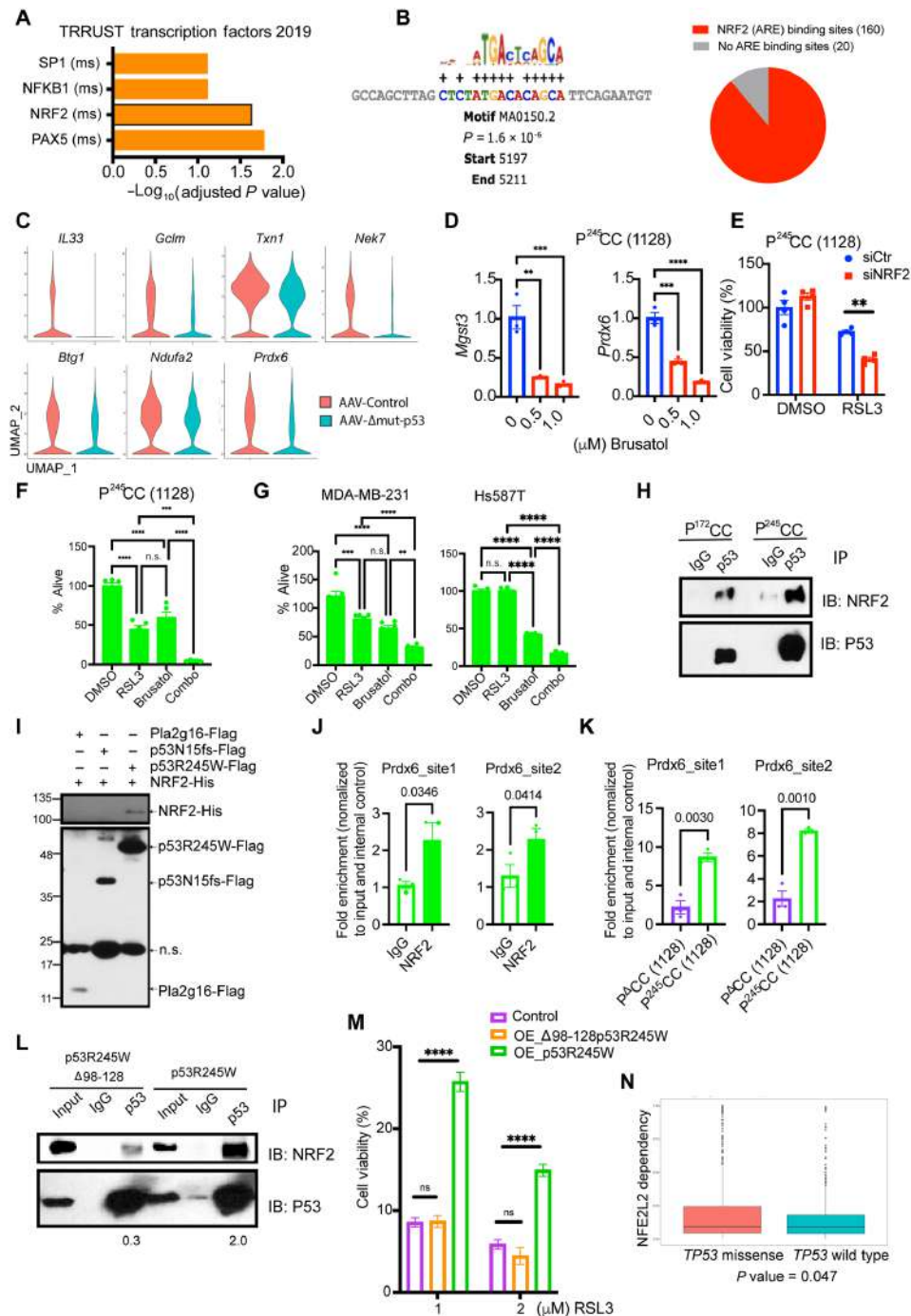
Fig. 6. Mutant p53 inhibits ferroptosis through the NRF2-dependent regulation of Mgst3 and Prdx6. (**A**) ENRICHR results for the top transcription factors of our mutant-p53/oxidative stress 6-gene dataset. (**B**) One hundred eighty DEGs regulated by mutant p53 in clusters 1, 9, 11, and 14 were examined for AREs. (**C**) Violin plots of seven DEGs from cancer clusters regulated by mutant p53 that contain AREs in their promoters. (**D**) RT-qPCR analysis for *Prdx6* and *Mgst3* in P[245]CC cells treated with brusatol for 3 hours. (**E**) Viability of P[245]CC cells with or without siRNA silencing of NRF2 and treated with RSL3 (10 μM) or DMSO. (**F**) Viability of P[245]CC cells treated with RSL3 (5 μM), brusatol (0.5 μM), or both (combo). (**G**) Cell viability of indicated cells treated with RSL3 (5 μM), brusatol (10 μM for MDA-MB-231 and 1.0 μM for HCC1395), or both. (**H**) Co-immunoprecipitation of mutant p53 and NRF2. IP, immunoprecipitation; IB, immunoblotting. (**I**) Purified NRF2-His bound p53R245W-Flag but not negative controls Pla2g16-Flag or p53N15fs-Flag (first 15 amino acids of p53, followed by a truncation and a frameshift). Membranes were probed with Flag and NRF2 antibodies. (**J** and **K**) CUT&RUN RT-qPCR for two ARE sequences within the *Prdx6* promoter using anti-NRF2 or immunoglobulin G (IgG) (J) or anti-p53 antibodies in P[245]CC cells (K). Cells with CRISPR knockout of mutant p53 were used as a baseline (K). (**L** and **M**) Co-immunoprecipitation of mutant p53 and NRF2 from lysates (L) and viability (M) in P[−/−]CC (1374) cells transduced with indicated lentiviruses. NRF2 pull-down was quantified as ratio of pull-down to input. (**N**) *NFE2L2* (NRF2) dependency of human cancer cell lines with missense *TP53* (*n* = 756) or wild type (*n* = 636). Data are means ± SEM. Significant differences were evaluated by Student's *t* test [(E), (J), and (K)] one-way ANOVA [(D), (F), (G), and (M)]. **$P < 0.01$, ***$P < 0.001$, and ****$P < 0.0001$.

from $Trp53^{fl/fl}$, $K14$-Cre, and $Rosa26^{LSL}$ $\underline{C}^{AS9\text{-}P2A\text{-}EGFP/+}$ mice. We now show that amino acids 98 to 128 are important for binding NRF2 as the ability of mutant p53 to bind NRF2 is diminished upon deletion of these sequences (Fig. 6L). In addition, overexpression of the mutant p53R245W in three different p53$^{-/-}$CC cell lines but not Δ98-128 p53R245W-rescued cells from RSL3-mediated cell death (Fig. 6M and fig. S6, H and I). Last, *Mgst3* and *Prdx6* transcript levels increased upon mutant p53R245W overexpression but not Δ98-128 p53R245W overexpression (fig. S6J). In summary, these data indicate that amino acids 98 to 128 of the mutant p53R245W are critical for the interaction with NRF2. Wild-type p53 also has the ability to bind NRF2 upon activation by irradiation (fig. S6K), the significance of which is unknown because our tumor cells only express mutant p53.

To further examine the functional implications of the interaction of mutant p53 with NRF2, we probed the DepMap (Cancer Dependency Map) database, which explores interdependencies. Mining the DepMap database revealed that NRF2 dependency was substantially enriched in human cancer cells lines with a *TP53* missense mutation compared to cell lines containing wild-type *TP53* (Fig. 6N), indicating that mutant p53/NRF2 interactions are meaningful in cancer cells. Cell lines with *TP53* truncations also showed dependency on NRF2 as compared to wild-type *TP53*, most likely from expressed truncated gene products (fig. S6L). Thus, mutant p53 mitigates ferroptosis through the NRF2-dependent regulation of *Mgst3* and *Prdx6*. In conclusion, mutant p53 protects breast adenocarcinomas against ferroptosis through interactions with NRF2 (fig. S7).

DISCUSSION

Here, we used a true somatic model of mutant p53 driven breast cancer that retains a wild-type p53 stroma and immune system. Tumors were driven by initiating hotspot p53 missense mutations, p53R172H or p53R245W, corresponding to p53R175H and p53R248W in patients. One major advantage of our model in comparison to the other models is that tumor evolution happens in a TME that retains wild-type p53. We found that TNBCs depend on mutant p53 for survival and that mutant p53 (two different mutants) protects cells from ferroptosis. The presence of large lipid droplets detected in hematoxylin and eosin (H&E) sections and by Red-Oil O staining, a phenotype observed in other ferroptosis studies, was the first indication that these cells died by ferroptosis (*36*). scRNA-seq analyses revealed, in an unbiased manner, the functional relevance of removing mutant p53 selectively in tumor cells and further implicated ferroptosis. Deletion of mutant p53 did not initiate apoptosis suggesting that other tumor-specific events prevent the cells from dying via apoptosis. Two other models also show mutant p53 dependency (lymphoma and colon carcinoma) (*13*, *14*). However, in these models, tamoxifen-driven deletion of mutant *Trp53* occurs in tumor cells and cells of the TME. The mechanisms for mutant p53 dependencies were not determined in these models. Last, the mechanism by which *p53*-null tumors bypass ferroptosis is unknown.

While the role of wild-type p53 in initiating ferroptosis is known, p53 hotspot mutants often have GOF activities that oppose wild-type functions (*8*, *37*, *38*). We uncovered that p53 missense mutations protect breast adenocarcinoma in vivo from ferroptosis mechanistically at the level of GPX4 thru NRF2. These findings are agnostic of p53R172H or p53R245W mutation in our murine breast cancer model and several additional hotspot *TP53* mutations analyzed in

human breast cancer cell lines. Thus, both structural and contact p53 missense mutants, which differ in how they lose DNA binding, protect cells from ferroptosis. Similarly, Su and colleagues (*39*) found that p53R172H has GOF properties that protects cells from ferroptosis but through abrogation of BTB and CNC homology 1 (BACH1)-dependent suppression of SLC7A11 in three tumor cell lines, a squamous cell carcinoma, a cholangiocarcinoma, and an endometrial carcinoma of the ovary. In contrast, Liu and colleagues (*40*) found that various mutant p53 hotspots do not protect but sensitize tumors to SLC7A11 inhibitors in esophageal cancer cell lines in vitro. Our p53 mutant breast tumors were also sensitive to SLC7A11 inhibitors, but tumors with mutant *Trp53* deletion were not. Instead, they are sensitive to RSL3 implicating intracellular mechanisms of ferroptosis. One additional important factor is that both BACH1 and NRF2 can compete for binding to AREs (*41*). Thus, BACH1 and NRF2 eventually target the same pathway and may be mutually exclusive events. Thus, context-specific mechanisms exist that are mutant and cancer/tissue specific. Additional studies are needed to understand these differences.

While the relationship between mutant p53 and oxidative stress was previously reported, the mechanisms by which mutant p53 regulated oxidative stress was unknown. Vermeulen *et al.* (*42*), using an in vivo model of tumor initiation in the intestine, found that p53R172H did not confer a benefit to colon stem cells under normal conditions but notably increased their fitness in the setting of colitis-associated ROS formation. Similarly, in an independent model of esophagus cancer, mutant p53 cells outcompeted wild-type cells following exposure to oxidative stress caused by low-dose ionizing radiation; however, antioxidant treatment given with low-dose ionizing radiation reversed this phenomenon and promoted the proliferation of wild-type cells over mutant cells, further confirming that mutant p53 mitigates ROS in vivo (*43*). Our study provides the bridge linking escape from ROS to protection from ferroptotic cell death via increasing levels of anti-ferroptotic enzymes.

Wild-type p53 can activate or inhibit ferroptosis that is context dependent (*38*, *44*). We used radiation to stabilize and activate wild-type p53 (normal cells have undetectable levels of p53) and show interactions with NRF2. Approximately 16% of TNBCs have wild-type *TP53* by sequence. Whether this p53 protein is stable in these tumors is unknown. Likely, this wild-type p53 is not functional as a tumor suppressor, perhaps through interactions with other proteins such as Mdm2, an E3 ligase that degrades p53, which is often overexpressed in breast cancers (*45*). Thus, although tumor cells may have wild-type p53, it may not be available to interact with NRF2. Meanwhile, mutant p53 protein is a very stable protein in cancer cells and can interact with other transcription factors such as NRF2 (*15*). Cancer cells whereby wild-type p53 activates p21 undergo cell cycle arrest and these cells are protected from ferroptosis by p21 (*44*). Regardless of being protected from ferroptosis, arrested cancer cells do not proliferate and thus do not contribute directly to tumor progression. Depletion of mutant *Trp53* in our tumor cells does not cause cell cycle arrest but induces cell death via ferroptosis, two very different outcomes.

Two independent GOF mechanisms attributed to mutant p53 in breast cancer, ferroptosis (this study) and the mevalonate pathway (*8*), are interconnected. GPX4 and ferroptosis suppressor protein 1 (FSP1) are two enzymes that act in parallel to inhibit ferroptosis. FSP1 targets coenzyme Q10 in the cell membrane and converts it to ubiquinol, a reduced form that protects cells against ferroptosis.

Coenzyme Q10, the substrate for FSP1, is the end product of the mevalonate pathway (*46*). Isopentenyl pyrophosphate, another by-product of the mevalonate pathway, contributes to the insertion of selenocysteine into the catalytic center of GPX4, a process important for GPX4 function (*47*). In summary, mutant p53 works on two fronts to halt breast cancer cells from undergoing ferroptosis. In the age of precision medicine, the dependency of breast cancers to mutant p53 via dampening ferroptosis offer additional opportunities for treating breast cancers with missense mutant p53.

MATERIALS AND METHODS

Mice

As previously described, $Trp53^{flox/flox}$ (*48*), $Trp53^{wm-R172H}$ (*49*), *K14-cre* (01XF1, NCI Repository), and $Rosa26^{LSL\ CAS9-P2A-EGFP/\ +}$ (024857, the Jackson Laboratories) (*50*) mice were bred and crossed in MD Anderson's Genetically Engineered Mouse Facility to generate $P^{172}CC$ and $P^{245}CC$ mice (*15*). All mice were bred and maintained in a mixed background (FVB, C57Bl/6, and BALB/c), and only female mice with mammary tumors were examined in the study. All mice were monitored daily. Animals with signs of physical distress or with large breast tumor volumes were euthanized. Tumor diameter was measured with calipers. At end point after euthanizing the mouse, we noticed that some of these spontaneous breast tumors invaginate internally (not visible), and true measurement was possible only on euthanasia upon dissection. Tumor volume was estimates using the formula (length × width^2) × π/8. All animal studies and procedures were approved by MD Anderson's Institutional Animal Care and Use Committee. Genotyping was carried out as described previously (*49*). Primer sequences are given in table S4. The rate of tumor growth was calculated using the formula ($V_{euth} - V_0$)/($T_{euth} - T_0$), where V_{euth} and T_{euth} are the tumor volume and treatment days, respectively, at the time of euthanasia; V_0 is the tumor volume at the start of treatment; and $T_0 = 0$.

Animal treatment

Once primary breast tumors reached approximately 0.8 cm in diameter, AAV virus particles ($5 × 10^9$ genome copies) suspended in 50 μl of sterile phosphate-buffered saline (PBS) were injected intratumorally. Tumors were injected with AAV on days 0, 3, and 8. For the liproxstatin-1 rescue experiment, animals were intraperitoneally injected with liproxstatin-1 (25 mg/kg; 17730, Cayman Chemicals) daily for 2 weeks. Liproxstatin-1 injections started on the same day as AAV injections.

To determine the functional significance of Mgst3 and Prdx6, $P^{245}CC$ (1128) cells expressing shRNA targeting *Mgst3*, *Prdx6*, or empty vector were grown in nude animals. A total of $5 × 10^5$ cancer cells suspended in 30 μl of PBS were injected into the mammary fat pad. Once tumors reached approximately 6 to 7 mm in diameter, all tumors were injected intratumorally with RSL3 (100 mg/kg; 19288, Cayman Chemicals), on days 0, 6, and 12. Tumor growth was monitored with caliper measurements of the length and width of the tumor. To determine the functional significance of MGST3 and PRDX6, human cell line MDA-MB-231 expressing shRNA targeting *MGST3*, *PRDX6*, or empty vector were grown in nude animals. MDA-MB-231 ($5 × 10^5$ or $3 × 10^6$) was suspended in 30 or 50 μl of PBS, respectively, and was injected into the mammary fat pad. Tumor growth was monitored with caliper measurements of the length and width of the tumor.

Cloning and virus production

Two sgRNAs targeting p53 that had been validated in vivo were used in this study (*50, 51*). As previously described, sgRNA 1 was inserted into an AAV plasmid ready for sgRNA cloning (PX552; RRID: Addgene_60958 deposited by F. Zhang in Addgene) (*15*). The same was done for sgRNA 2. Subsequently, polymerase chain reaction (PCR) amplification of the U6 promoter–driven sgRNA 2 was subcloned into the vector containing sgRNA 1, so that each AAV plasmid had two sgRNAs. Two nontargeting sgRNAs were similarly cloned and used as controls. The sequences of the guides are given in table S2. Plasmids were confirmed by Sanger sequencing. High-titer and pure AAV8 viruses were generated by the Gene Vector Core at Baylor College of Medicine. Virus was titered using real-time quantitative PCR (qPCR). Each tumor was injected with $5 × 10^9$ total genome copies. High-titer AAV8-EF1-tdTomato-WPRE-hGH (AAV-tdTomato; $2.6 × 10^{13}$ genome copies/ml) was purchased from Gene Vector Core.

The flag-tagged R245W and p53N15fs (cDNA deletion by Sac I digestion and relegation to change the reading frame of p53) were cloned into pBABE-IRES-EGFP-puro retrovirus vector. pLV-CMV-hismNrf2-T2A-EGFP-Puro was purchased from VectorBuilder, and pBABE-flag-Pla2g16 was previously published from our group (*9*). Plasmids were confirmed by Sanger sequencing.

The *Mgst3* and *Prdx6* cDNAs were purchased from Addgene (Origene, MR201107 and MR202605), and each cDNA was cloned into a pLVX-IRES-EGFP lentiviral vector (Addgene, 128652) via Eco RI/Xba I sites by replacing green fluorescent protein (GFP) in the lentivirus backbone. Plasmids were confirmed by Sanger sequencing. Doxycycline-inducible sgRNA lentiviral vectors targeting p53 at exons 4 and 5 and control vectors, deposited by Marco Heraldo's laboratory (*19*), were used to conditionally delete mutant p53 (Addgene, 70183, 85534, and 85535). The sequence of mutant p53 R245W cDNA lacking amino acids 98 to 128 were synthesized by TwistBioscience. p53 cDNA from pLV-CMV-Trp53R245W-EF1A-EGFP:T2A:Puro plasmid purchased from VectorBuilder was cleaved out by enzymes Bam H1 and Sal 1 and replaced by the synthesized Δ98-128 p53R245W. Plasmids were confirmed by Sanger sequencing.

Lentiviral-overexpressing plasmids were packaged into lentiviral particles and infected into breast tumor cell lines. Stably integrated overexpressing plasmids were selected by adding puromycin (2 μg/ml; Invitrogen) to culture media for 3 days. These pools of selected cells were used for experiments.

Cell lines

Primary murine breast cancer cell lines ($P^{172}CC$ and $P^{245}CC$) were generated by mincing breast tumors into 1-mm^3 fragments, which were subjected to trypsinization for 20 min at 37°C and then cultured in Dulbecco's modified Eagle's medium (DMEM) supplemented with 10% fetal bovine serum (FBS) and 1% penicillin/streptomycin. P53R245W (391) is an adenocarcinoma breast cancer cell originating from a germline *Trp53-wm245* animal. Cells were passaged no more than 12 to 20 times before the completion of the experiments. Human breast cancer cell Hs587T, HCC38 (RRID:CVCL_1267), and HCC1395 (RRID:CVCL_1249) were purchased from American Type Culture Collection (ATCC) before performing the experiments. The other human breast tumor cells lines were purchased from MD Anderson's Cytogenetics and Cell Authentication Core and verified by DNA fingerprinting. All cells were cultured in DMEM supplemented with 10% FBS and 1% penicillin/streptomycin. All cell lines

were routinely confirmed by PCR to be negative for mycoplasma. CRISPR knockout clones were established by treating P^{172}CC or P^{245}CC parental cells with AAV-mut-p53 for 48 hours and subsequently seeding one cell per well in a 96-well plate. The clones were validated with Western blotting.

Red Oil O stain
Red Oil O staining was performed by MD Anderson's Department of Veterinary Medicine and Surgery's histology laboratory using a Red Oil O staining kit (ORK-1-IFU, ScyTek Laboratories) kit according to the manufacturer's instructions.

In vitro experiments
Cells (1×10^4) were seeded in a 96-well plate. The next day, the cells were treated with the indicated agents RSL3 (#19288, Cayman Chemicals), erastin (#17754s, Cayman Chemicals), ML210 (#S0788; SelleckChem), ML162 (#S4452; SelleckChem), and liproxstatin-1 (#7699, SelleckChem) for 24 hours, and cell viability was assessed with an MTT [3-(4, 5-dimethylthiazolyl-2)-2, 5-diphenyltetrazolium bromide] colorimetric assay. For the combination of liproxstatin-1 and ferroptosis activators, liproxstatin-1 was added 30 min before the activators. For the combination of brusatol and RSL3 experiments, brusatol was added 3 hours before adding RSL3. For reverse transcription qPCR (RT-qPCR) experiments, cells seeded 24 hours before treatment with brusatol for 3 hours or luteolin (S2320, SelleckChem) for 24 hours with varying concentrations as indicated in figure legends.

Lipid ROS measurement
Cells (5×10^5) were plated in six-well plates and treated the next day with RSL3 (19288, Cayman Chemicals) or dimethyl sulfoxide for 3 hours. The cells were then incubated with 1.5 µM C11-BODIPY 581/591 (Thermo Fisher Scientific) for 20 to 30 min at 37°C. For C11-BODIPY 581/591 staining, the signals from both nonoxidized C11 [phycoerythrin (PE) channel] and oxidized C11 [fluorescein isothiocyanate (FITC) channel] were measured. The ratio of the mean fluorescence intensity of FITC to that of PE was calculated for each sample.

Short interfering RNA and lentivirus shRNA-mediated gene silencing
The short interfering RNAs (siRNAs) used in this study were murine *Trp53* (MilliporeSigma, SASI_00310137), human *TP53* (Dharmacon, ON-TARGETplus siRNA L-003329-00-0005), murine *Nfe2l2* (Dharmacon, D040766-01-0005 and D040766-03-0005), murine *Mgst3* (MilliporeSigma, SASI_00129357 and SASI_00129358), murine *Prdx6* (MilliporeSigma, SASI_00136163 and SASI_00136164), and MISSION siRNA Universal Negative Control (MilliporeSigma). Cells (4×10^5) were seeded in a six-well plate. siRNA (20 µM) and Lipofectamine RNAiMAX transfection reagent (Thermo Fisher Scientific) were mixed according to the manufacturer's instructions and added to 250 µl of serum-free medium for 15 min. The transfection mixture was then combined with 1 ml of fresh culture medium and added to the cells. Twenty-four hours later, cells were trypsinized and plated in a 6-cm dish, so that the cell confluence remains less than 70% when cells are harvested for RT-qPCR. Gene silencing relative to control was measured 48 hours after transfection by RT-qPCR. shRNA glycerol stocks that contained pGIPZ-GFP expressing shRNA against mouse *Mgst3* and *Prdx6* as well as human *MGST3* and *PRDX6* were

obtained from the MDACC Functional Genomic Core (see table S2). Lentiviral shRNA plasmids were packaged into lentiviral particles and infected into murine and human cell lines. Stably integrated shRNAs were selected by adding puromycin (2 to 3 µg/ml; Invitrogen) to culture medium for 2 days.

Cut and run chromatin profiling
The CUT&RUN Assay Kit from Cell Signaling Technology (86652) was used according to manufacturer's instructions. For each reaction, 150,000 cells P^{245}CC were used. A 1 µg of NRF2 [Cell Signaling Technology, catalog no. 12721 (also 12721S and 12721T), RRID:AB_2715528] or rabbit immunoglobulin G (IgG) were (Cell Signaling Technology, catalog no. 2729, RRID:AB_1031062) were used per each reaction. CM5 rabbit anti-p53 (2 µl; CM5, Leica Biosystems) was used in cells with mutant p53 (P^{245}CC,1128) or in isogenic mut-p53 CRISPR KO (P^{245}CC,1128) cells. To determine whether NRF2 and mut-p53 bind two independent ARE sites in the Prdx6 promoter, lysates were probed via RT-qPCR with primers specific for each ARE site. The RT-qPCR primer sequences are listed in table S2.

Immunoprecipitation and immunoblotting
For immunoprecipitation, cells were lysed with a nondenaturing buffer [50 mM tris HCl (pH 7.4), 150 mM NaCl, 1% NP-40, and 2 mM EDTA containing protease and phosphatase inhibitors (Santa Cruz Biotechnology)]. Immunoprecipitations with 2 µl of rabbit anti-p53 (CM5, Leica Biosystems) or rabbit IgG (Cell Signaling Technology) primary antibodies and 1 mg of total protein lysates were performed overnight at 4°C. Cells used for immunoprecipitation were pretreated with 5 µM MG132 (C2211, MilliporeSigma) overnight. The next morning, the lysates were incubated with 20 µl of Protein A Dynabeads (10001, Thermo Fisher Scientific) for 3 hours at 4°C. The beads were subsequently washed four times and heated to 95°C for 5 min in 35 µl of sample buffer. For immunoblotting, equal amounts of protein from each sample were subjected to SDS–polyacrylamide gel electrophoresis (SDS-PAGE) and transferred to ImmunBlot polyvinylidene difluoride membranes (Bio-Rad). The following antibodies were used: anti-NRF2 [Cell Signaling Technology, catalog no. 12721 (also 12721S, 12721 T), RRID:AB_2715528], anti-p53 (for mouse samples; Leica Biosystems, catalog no. NCL-p53-CM5p, RRID:AB_563933), anti-p53 (for human samples; FL-393, Santa Cruz Biotechnology), anti–glyceraldehyde-3-phosphate dehydrogenase (GAPDH) [Cell Signaling Technology, catalog no. 2118 (also 2118 L), RRID:AB_561053], anti-vinculin (MilliporeSigma, catalog no. V9131, RRID:AB_477629), VeriBlot–horseradish peroxidase (Abcam, catalog no. ab131366, RRID:AB_2892718), and anti–β-actin (MilliporeSigma catalog no. A2228, RRID:AB_476697). The flag-tagged p53 R245W, p53N15fs, and Pla2g16 were transfected into 293T cells. The cell pellets were briefly sonicated in PBS buffer with protease inhibitor cocktail (MilliporeSigma, 11697498001), and the supernatants were incubated with Anti-FlagM2 affinity gel (Millipore, A2220) for 60 min, and washed three times. pLV-CMV-hismNrf2-T2AEGFP-Puro plasmid was purchased from VectorBuilder (Chicago, IL) and transfected in 293T cells. To test binding of p53 proteins with NRF2 in vitro, cell lysates containing his-tag mouse NRF2 were purified by HisPur Ni-NTA resin (88221, Thermo Fisher Scientific) according to the manufacturer's instructions and then added to Anti-FlagM2 affinity gel bound pp53R245W, p53N15fs, or Pla2g16 proteins and incubated for 1 hour with 10 µM Z-VAD-FMK (Selleckchem, S7023). The mixtures were washed three

times, and then Western blots were performed using NRF2 antibody (Thermo Fisher Scientific, catalog no. PA5-27882, RRID:AB_2545358) and Flag-tag (Invitrogen, MA1-142) antibodies.

Histopathology and immunohistochemistry
As previously described, tissues harvested from mice were fixed in 10% neutral buffered formalin saline and embedded in paraffin (15). Tissues were processed, embedded in paraffin, cut into 5-μm sections, and subjected to H&E staining in MD Anderson's Department of Veterinary Medicine and Surgery's histology laboratory. Immunohistochemistry was performed using standard methods with citrate buffer for 30 min of antigen retrieval. Slides were stained with antibodies against cleaved caspase-3 [Cell Signaling Technology, catalog no. 9664 (also 9664P), RRID:AB_2070042] and 4HNE (Abcam, catalog no. ab46545, RRID:AB_722490). Visualization was performed using biotinylated secondary antibody kits (VECTASTAIN ABC and DAB kits, Vector Laboratories), with hematoxylin as the counterstain.

Immunofluorescence
As previously described, paraffin-embedded tumor sections were deparaffinized and rehydrated, and antigen retrieval was performed in tris-EDTA (pH 9.0). Slides were blocked in PBS containing 3% fish gelatin (VWR) for 20 min (15). Tissue sections were incubated with an anti-p53 antibody (Leica Biosystems, catalog no. NCL-p53-CM5p, RRID:AB_563933; 1:200) and pSTING Ser^{366} (1:100; 19781S, Cell Signaling Technology) overnight at 4°C and then incubated with a secondary antibody labeled with anti-rabbit Alexa Fluor 555 (Thermo Fisher Scientific, catalog no. A-21428, RRID:AB_2535849, 1:600). The sections were counterstained with 4′,6-diamidino-2-phenylindole (Thermo Fisher Scientific). Images were acquired using a Nikon 80i upright widefield fluorescence microscope with NIS-Elements imaging software.

RNA extraction
As previously described, flash-frozen tissue was pulverized, and total RNA was prepared using TRIzol reagent (Invitrogen) and purified using the RNeasy mini kit (QIAGEN) (15). Briefly, the homogenized tissues were incubated with 500 μl of TRIzol at room temperature for 5 min. Chloroform was then added to the tissue/TRIzol mixture (chloroform:TRIzol, 1:5 in volume) and mixed by vortex mixing. The chloroform/tissue/TRIzol mixture was incubated at room temperature for 3 min and then centrifuged at 12,000g for 30 min at 4°C. The upper phase was transferred to a new tube; 1.5 volumes of 100% ethanol were added to the upper phase, and this combination was mixed thoroughly by inverting the tube several times and then loaded into the RNeasy spin column (QIAGEN) as per the manufacturer's protocol.

RT-qPCR
RNA was purified as described above. cDNA was synthesized using the iScript Reverse Transcription Supermix Kit (Bio-Rad). Quantitative PCR was performed with CFX96 (Bio-Rad), and data were analyzed using CFX Maestro Software (Bio-Rad). mRNA levels were calculated using the ΔCt method and normalized to those of large ribosomal protein (RPLP0). Results are expressed as fold changes relative to the controls. The RT-qPCR primer sequences are listed in table S2.

Statistical analysis
All data are presented as means ± SEM. GraphPad Prism 9.0 was used to perform all statistical analyses. Statistical significance was evaluated with the Student's t test or analysis of variance (ANOVA) as appropriate. $P < 0.05$ was considered significant. A log-rank Mantel-Cox test was used to compare survival curves.

scRNA-seq and analysis
Fresh murine breast tumors were dissociated into single cells as described previously (52). A mixture of all cells from the breast tumors (including TME, 1×10^4) were subjected to scRNA-seq with the Chromium Controller system (10x Genomics) at MD Anderson's Cancer Prevention and Research Institute of Texas (CPRIT) SINGLE CORE. Libraries were sequenced with the Illumina NovaSeq 6000 system at MD Anderson's Advanced Technology Genomics Core.

We sequenced 5000 to 10,000 cells per sample; the mean reads per cell ranged from 37,000 to 124,000, and the median number of genes per cell was >1200. Raw scRNA-seq data were preprocessed, demultiplexed, and aligned to a mouse reference genome (GRCm38) using 10x Genomics Cellranger DNA (RRID:SCR_023221). Cells with <200 genes or >6000 genes [likely doublets or multiplets as predicted by Scrublet (RRID:SCR_018098)] and cells with >30% of the read counts derived from the mitochondrial genome were removed (53). The batch effect was corrected by Harmony algorithm in Seurat v4 (54, 55). Raw unique molecular identifier counts were log-normalized and used for principal components analysis. Seurat v4 was applied to the normalized gene-cell matrix to identify highly variable genes for unsupervised cell clustering (55). For visualization, the dimensionality was further reduced using the UMAP method (56).

To define the major cell type and state of each single cell, we identified the DEGs for each cell cluster and used the top most significant DEGs to annotate each cluster with GSEA. We identified DEGs for cell subpopulations of interest using Seurat, and DEGs were filtered to select significant DEGs [log$_2$ fold change >1.0 or <−1.0 and false discovery rate (FDR) q value < 0.05] between two conditions. For pathway analysis, the curated gene sets (including the Hallmark, GO, KEGG, and REACTOME gene sets) were downloaded from the Molecular Signature Database. Single-sample GSVA (GSVA, RRID:SCR_021058) was applied, and pathway scores for each cell type were calculated using the GSVA software package (22). GSVA is a GSEA method that estimates variation of pathway activity over a sample population in an unsupervised manner. GSEA was performed to identify significantly enriched signaling pathways (FDR q value < 0.01) between two conditions (20). MEME Motif Aligment & Search Tool was used to search promoters (10 kb upstream of starting site) of 180 DEGs enriched in epithelial cluster (1, 9, 11, 14) in mutant p53 on (AAV-Control) when compared to cancer cells from AAV-Δmut-p53 for NRF2-binding sites (ARE sites) (57). An E value of 10 was used to score the hits. NRF2 motif Matrix ID MA0150.2 from JASPAR2022 was used to scan promoters.

DepMap analysis
We filtered the OmicsSomaticMutations.csv to only return cell lines with missense mutations in TP53, truncations, or wild-type TP53. Wild-type TP53 was defined as any sample without any kind of mutation in the TP53 gene. Next, we used the CRISPRGeneDependency.csv file from DeepMap to select the gene dependency on results based on NFE2L2 gene stratified by TP53 status. We performed a Wilcoxon signed rank test to compare gene dependency for NFE2L2 comparing missense mutation in TP53 versus wild type. Results were visualized by creating boxplots of the gene dependencies.

Analysis of invasive breast carcinomas in TCGA

FASTQ files for breast samples in TCGA were aligned to a mouse reference genome (GRCh38) by STAR (RRID:SCR_005622) to generate RNA-seq BAM files (58). STAR was used to summarize aligned reads at the gene level to generate the raw count data, which were processed and normalized with DESeq2 (RRID:SCR_015687) software (58, 59). Samples with *TP53* missense mutations and samples with truncating mutations were subjected to GSEA (RRID:SCR_003199). We evaluated gene sets (including the Hallmark, GO, KEGG, and REACTOME gene sets) from the Molecular Signature Database to identify significantly enriched gene sets and pathways. Gene Expression Profiling Interactive Analysis (GEPIA2, RRID:SCR_018294) was used to perform the survival analysis based on gene signature (60).

Supplementary Materials

This PDF file includes:
Figs. S1 to S7
Legends for tables S1 to S4

Other Supplementary Material for this manuscript includes the following:
Tables S1 to S4

REFERENCES AND NOTES

1. H. Ying, A. C. Kimmelman, C. A. Lyssiotis, S. Hua, G. C. Chu, E. Fletcher-Sananikone, J. W. Locasale, J. Son, H. Zhang, J. L. Coloff, H. Yan, W. Wang, S. Chen, A. Viale, H. Zheng, J. H. Paik, C. Lim, A. R. Guimaraes, E. S. Martin, J. Chang, A. F. Hezel, S. R. Perry, J. Hu, B. Gan, Y. Xiao, J. M. Asara, R. Weissleder, Y. A. Wang, L. Chin, L. C. Cantley, R. A. DePinho, Oncogenic Kras maintains pancreatic tumors through regulation of anabolic glucose metabolism. *Cell* **149**, 656–670 (2012).

2. D. C. Koboldt, Cancer Genome Atlas Network, Comprehensive molecular portraits of human breast tumours. *Nature* **490**, 61–70 (2012).

3. L. Aschauer, P. A. Muller, Novel targets and interaction partners of mutant p53 gain-of-function. *Biochem. Soc. Trans.* **44**, 460–466 (2016).

4. M. P. Kim, G. Lozano, Mutant p53 partners in crime. *Cell Death Differ.* **25**, 161–168 (2018).

5. G. A. Lang, T. Iwakuma, Y. A. Suh, G. Liu, V. A. Rao, J. M. Parant, Y. A. Valentin-Vega, T. Terzian, L. C. Caldwell, L. C. Strong, A. K. el-Naggar, G. Lozano, Gain of function of a p53 hot spot mutation in a mouse model of Li-Fraumeni syndrome. *Cell* **119**, 861–872 (2004).

6. M. P. Kim, X. Li, J. Deng, Y. Zhang, B. Dai, K. L. Allton, T. G. Hughes, C. Siangco, J. J. Augustine, Y. Kang, J. M. McDaniel, S. Xiong, E. J. Koay, F. McAllister, C. A. Bristow, T. P. Heffernan, A. Maitra, B. Liu, M. C. Barton, A. R. Wasylishen, J. B. Fleming, G. Lozano, Oncogenic KRAS recruits an expansive transcriptional network through mutant p53 to drive pancreatic cancer metastasis. *Cancer Discov.* **11**, 2094–2111 (2021).

7. W. A. Freed-Pastor, C. Prives, Mutant p53: One name, many proteins. *Genes Dev.* **26**, 1268–1286 (2012).

8. W. A. Freed-Pastor, H. Mizuno, X. Zhao, A. Langerød, S. H. Moon, R. Rodriguez-Barrueco, A. Barsotti, A. Chicas, W. Li, A. Polotskaia, M. J. Bissell, T. F. Osborne, B. Tian, S. W. Lowe, J. M. Silva, A. L. Børresen-Dale, A. J. Levine, J. Bargonetti, C. Prives, Mutant p53 disrupts mammary tissue architecture via the mevalonate pathway. *Cell* **148**, 244–258 (2012).

9. S. B. Xiong, H. Tu, M. Kollareddy, V. Pant, Q. Li, Y. Zhang, J. G. Jackson, Y.-A. Suh, A. C. Elizondo-Fraire, P. Yang, G. Chau, M. Tashakori, A. R. Wasylishen, Z. Ju, H. Solomon, V. Rotter, B. Liu, A. K. El-Naggar, L. A. Martinez, G. Lozano, Pla2g16 phospholipase mediates gain-of-function activities of mutant p53. *P Natl Acad Sci USA* **111**, 11145–11150 (2014).

10. M. Adorno, M. Cordenonsi, M. Montagner, S. Dupont, C. Wong, B. Hann, A. Solari, S. Bobisse, M. B. Rondina, V. Guzzardo, A. R. Parenti, A. Rosato, S. Bicciato, A. Balmain, S. Piccolo, A Mutant-p53/Smad Complex Opposes p63 to Empower TGFβ-Induced Metastasis. *Cell* **137**, 87–98 (2009).

11. E. Kotler, O. Shani, G. Goldfeld, M. Lotan-Pompan, O. Tarcic, A. Gershoni, T. A. Hopf, D. S. Marks, M. Oren, E. Segal, A systematic p53 mutation library links differential functional impact to cancer mutation pattern and evolutionary conservation. *Mol. Cell* **71**, 873 (2018).

12. A. O. Giacomelli, X. Yang, R. E. Lintner, J. M. McFarland, M. Duby, J. Kim, T. P. Howard, D. Y. Takeda, S. H. Ly, E. Kim, H. S. Gannon, B. Hurhula, T. Sharpe, A. Goodale, B. Fritchman, S. Steelman, F. Vazquez, A. Tsherniak, A. J. Aguirre, J. G. Doench, F. Piccioni, C. W. M. Roberts, W. C. Hahn, M. Meyerson, G. Getz, C. M. Johannessen, D. E. Root, W. C. Hahn, Mutational processes shape the landscape of TP53 mutations in human cancer. *Nat. Genet.* **50**, 1381–1387 (2018).

13. E. M. Alexandrova, A. R. Yallowitz, D. Li, S. Xu, R. Schulz, D. A. Proia, G. Lozano, M. Dobbelstein, U. M. Moll, Erratum: Corrigendum: Improving survival by exploiting tumour dependence on stabilized mutant p53 for treatment. *Nature* **527**, 398 (2015).

14. R. Schulz-Heddergott, N. Stark, S. J. Edmunds, J. Li, L. C. Conradi, H. Bohnenberger, F. Ceteci, F. R. Greten, M. Dobbelstein, U. M. Moll, Therapeutic ablation of gain-of-function mutant p53 in colorectal cancer inhibits Stat3-mediated tumor growth and invasion. *Cancer Cell* **34**, 298–314.e7 (2018).

15. D. Dibra, S. M. Moyer, A. K. el-Naggar, Y. Qi, X. Su, G. Lozano, Triple-negative breast tumors are dependent on mutant p53 for growth and survival. *Proc. Natl. Acad. Sci. U.S.A.* **120**, e2308807120 (2023).

16. W. Wang, M. Green, J. E. Choi, M. Gijón, P. D. Kennedy, J. K. Johnson, P. Liao, X. Lang, I. Kryczek, A. Sell, H. Xia, J. Zhou, G. Li, J. Li, W. Li, S. Wei, L. Vatan, H. Zhang, W. Szeliga, W. Gu, R. Liu, T. S. Lawrence, C. Lamb, Y. Tanno, M. Cieslik, E. Stone, G. Georgiou, T. A. Chan, A. Chinnaiyan, W. Zou, CD8(+) T cells regulate tumour ferroptosis during cancer immunotherapy. *Nature* **569**, 270–274 (2019).

17. J. M. Ubellacker, A. Tasdogan, V. Ramesh, B. Shen, E. C. Mitchell, M. S. Martin-Sandoval, Z. Gu, M. L. McCormick, A. B. Durham, D. R. Spitz, Z. Zhao, T. P. Mathews, S. J. Morrison, Lymph protects metastasizing melanoma cells from ferroptosis. *Nature* **585**, 113–118 (2020).

18. M. Weiwer et al., Development of small-molecule probes that selectively kill cells induced to express mutant RAS. *Bioorg. Med. Chem. Lett.* **22**, 1822–1826 (2012).

19. B. J. Aubrey, G. L. Kelly, A. J. Kueh, M. S. Brennan, L. O'Connor, L. Milla, S. Wilcox, L. Tai, A. Strasser, M. J. Herold, An inducible lentiviral guide RNA platform enables the identification of tumor-essential genes and tumor-promoting mutations in vivo. *Cell Rep.* **10**, 1422–1432 (2015).

20. A. Subramanian, P. Tamayo, V. K. Mootha, S. Mukherjee, B. L. Ebert, M. A. Gillette, A. Paulovich, S. L. Pomeroy, T. R. Golub, E. S. Lander, J. P. Mesirov, Gene set enrichment analysis: A knowledge-based approach for interpreting genome-wide expression profiles. *Proc. Natl. Acad. Sci. U.S.A.* **102**, 15545–15550 (2005).

21. M. Xu, J. Tao, Y. Yang, S. Tan, H. Liu, J. Jiang, F. Zheng, B. Wu, Ferroptosis involves in intestinal epithelial cell death in ulcerative colitis. *Cell Death Dis.* **11**, 86 (2020).

22. S. Hanzelmann, R. Castelo, J. Guinney, GSVA: Gene set variation analysis for microarray and RNA-seq data. *BMC Bioinformatics* **14**, 7 (2013).

23. B. Lu, X. B. Chen, Y. C. Hong, H. Zhu, Q. J. He, B. Yang, M. D. Ying, J. Cao, Identification of PRDX6 as a regulator of ferroptosis. *Acta Pharmacol. Sin.* **40**, 1334–1342 (2019).

24. A. B. Fisher, J. P. Vasquez-Medina, C. Dodia, E. M. Sorokina, J. Q. Tao, S. I. Feinstein, Peroxiredoxin 6 phospholipid hydroperoxidase activity in the repair of peroxidized cell membranes. *Redox Biol.* **14**, 41–46 (2018).

25. P. J. Jakobsson, J. A. Mancini, D. Riendeau, A. W. Ford-Hutchinson, Identification and characterization of a novel microsomal enzyme with glutathione-dependent transferase and peroxidase activities. *J. Biol. Chem.* **272**, 22934–22939 (1997).

26. A. Chiba, N. Kawabata, M. Yamaguchi, S. Tokonami, I. Kashiwakura, Regulation of antioxidant stress-responsive transcription factor nrf2 target gene in the reduction of radiation damage by the thrombocytopenia drug romiplostim. *Biol. Pharm. Bull.* **43**, 1876–1883 (2020).

27. L. Gao, V. Kumar, N. N. Vellichirammal, S. Y. Park, T. L. Rudebush, L. Yu, W. M. Son, E. J. Pekas, A. M. Wafi, J. Hong, P. Xiao, C. Guda, H. J. Wang, H. D. Schultz, I. H. Zucker, Functional, proteomic and bioinformatic analyses of Nrf2- and Keap1- null skeletal muscle. *J. Physiol.* **598**, 5427–5451 (2020).

28. W. Li, M. Febbraio, S. P. Reddy, D. Y. Yu, M. Yamamoto, R. L. Silverstein, CD36 participates in a signaling pathway that regulates ROS formation in murine VSMCs. *J. Clin. Invest.* **120**, 3996–4006 (2010).

29. C. Cobaleda, A. Schebesta, A. Delogu, M. Busslinger, Pax5: The guardian of B cell identity and function. *Nat. Immunol.* **8**, 463–470 (2007).

30. M. Rojo de la Vega, E. Chapman, D. D. Zhang, NRF2 and the Hallmarks of Cancer. *Cancer Cell* **34**, 21–43 (2018).

31. D. Walerych, K. Lisek, R. Sommaggio, S. Piazza, Y. Ciani, E. Dalla, K. Rajkowska, K. Gaweda-Walerych, E. Ingallina, C. Tonelli, M. J. Morelli, A. Amato, V. Eterno, A. Zambelli, A. Rosato, B. Amati, J. R. Wiśniewski, G. del Sal, Proteasome machinery is instrumental in a common gain-of-function program of the p53 missense mutants in cancer. *Nat. Cell Biol.* **18**, 897–909 (2016).

32. K. Lisek, E. Campaner, Y. Ciani, D. Walerych, G. Del Sal, Mutant p53 tunes the NRF2-dependent antioxidant response to support survival of cancer cells. *Oncotarget* **9**, 20508–20523 (2018).

33. D. Malhotra, E. Portales-Casamar, A. Singh, S. Srivastava, D. Arenillas, C. Happel, C. Shyr, N. Wakabayashi, T. W. Kensler, W. W. Wasserman, S. Biswal, Global mapping of binding sites for Nrf2 identifies novel targets in cell survival response through ChIP-Seq profiling and network analysis. *Nucleic Acids Res.* **38**, 5718–5734 (2010).

34. S. Chian, R. Thapa, Z. Chi, X. J. Wang, X. Tang, Luteolin inhibits the Nrf2 signaling pathway and tumor growth in vivo. *Biochem. Biophys. Res. Commun.* **447**, 602–608 (2014).

35. A. Olayanju, I. M. Copple, H. K. Bryan, G. T. Edge, R. L. Sison, M. W. Wong, Z. Q. Lai, Z. X. Lin, K. Dunn, C. M. Sanderson, A. F. Alghanem, M. J. Cross, E. C. Ellis, M. Ingelman-Sundberg,

H. Z. Malik, N. R. Kitteringham, C. E. Goldring, B. K. Park, Brusatol provokes a rapid and transient inhibition of Nrf2 signaling and sensitizes mammalian cells to chemical toxicity-implications for therapeutic targeting of Nrf2. *Free Radic. Biol. Med.* **78**, 202–212 (2015).

36. M. A. Badgley, D. M. Kremer, H. C. Maurer, K. E. DelGiorno, H. J. Lee, V. Purohit, I. R. Sagalovskiy, A. Ma, J. Kapilian, C. E. M. Firl, A. R. Decker, S. A. Sastra, C. F. Palermo, L. R. Andrade, P. Sajjakulnukit, L. Zhang, Z. P. Tolstyka, T. Hirschhorn, C. Lamb, T. Liu, W. Gu, E. S. Seeley, E. Stone, G. Georgiou, U. Manor, A. Iuga, G. M. Wahl, B. R. Stockwell, C. A. Lyssiotis, K. P. Olive, Cysteine depletion induces pancreatic tumor ferroptosis in mice. *Science* **368**, 85–89 (2020).

37. S. H., p53 Represses the Mevalonate Pathway to Mediate Tumor Suppression. *Cell* **176**, 564–580.e19 (2019).

38. L. Jiang, N. Kon, T. Li, S. J. Wang, T. Su, H. Hibshoosh, R. Baer, W. Gu, Ferroptosis as a p53-mediated activity during tumour suppression. *Nature* **520**, 57–62 (2015).

39. Z. Su, N. Kon, J. Yi, H. Zhao, W. Zhang, Q. Tang, H. Li, H. Kobayashi, Z. Li, S. Duan, Y. Liu, K. P. Olive, Z. Zhang, B. Honig, J. J. Manfredi, A. K. Rustgi, W. Gu, Specific regulation of BACH1 by the hotspot mutant p53(R175H) reveals a distinct gain-of-function mechanism. *Nat Cancer* **4**, 564–581 (2023).

40. D. S. Liu, C. P. Duong, S. Haupt, K. G. Montgomery, C. M. House, W. J. Azar, H. B. Pearson, O. M. Fisher, M. Read, G. R. Guerra, Y. Haupt, C. Cullinane, K. G. Wiman, L. Abrahmsen, W. A. Phillips, N. J. Clemons, Inhibiting the system x(C)(−)/glutathione axis selectively targets cancers with mutant-p53 accumulation. *Nat. Commun.* **8**, 14844 (2017).

41. H. Nishizawa, M. Yamanaka, K. Igarashi, Ferroptosis: Regulation by competition between NRF2 and BACH1 and propagation of the death signal. *FEBS J.* **290**, 1688–1704 (2023).

42. L. Vermeulen, E. Morrissey, M. van der Heijden, A. M. Nicholson, A. Sottoriva, S. Buczacki, R. Kemp, S. Tavaré, D. J. Winton, Defining Stem Cell Dynamics in Models of Intestinal Tumor Initiation. *Science* **342**, 995–998 (2013).

43. D. Fernandez-Antoran, G. Piedrafita, K. Murai, S. H. Ong, A. Herms, C. Frezza, P. H. Jones, Outcompeting p53-mutant cells in the normal esophagus by redox manipulation. *Cell Stem Cell* **25**, 329–341.e6 (2019).

44. A. Tarangelo, L. Magtanong, K. T. Bieging-Rolett, Y. Li, J. Ye, L. D. Attardi, S. J. Dixon, p53 Suppresses metabolic stress-induced ferroptosis in cancer cells. *Cell Rep.* **22**, 569–575 (2018).

45. S. Haupt, R. Vijayakumaran, P. J. Miranda, A. Burgess, E. Lim, Y. Haupt, The role of MDM2 and MDM4 in breast cancer development and prevention. *J. Mol. Cell Biol.* **9**, 53–61 (2017).

46. K. Bersuker, J. M. Hendricks, Z. Li, L. Magtanong, B. Ford, P. H. Tang, M. A. Roberts, B. Tong, T. J. Maimone, R. Zoncu, M. C. Bassik, D. K. Nomura, S. J. Dixon, J. A. Olzmann, The CoQ oxidoreductase FSP1 acts parallel to GPX4 to inhibit ferroptosis. *Nature* **575**, 688–692 (2019).

47. V. S. Viswanathan, M. J. Ryan, H. D. Dhruv, S. Gill, O. M. Eichhoff, B. Seashore-Ludlow, S. D. Kaffenberger, J. K. Eaton, K. Shimada, A. J. Aguirre, S. R. Viswanathan, S. Chattopadhyay, P. Tamayo, W. S. Yang, M. G. Rees, S. Chen, Z. V. Boskovic, S. Javaid, C. Huang, X. Wu, Y. Y. Tseng, E. M. Roider, D. Gao, J. M. Cleary, B. M. Wolpin, J. P. Mesirov, D. A. Haber, J. A. Engelman, J. S. Boehm, J. D. Kotz, C. S. Hon, Y. Chen, W. C. Hahn, M. P. Levesque, J. G. Doench, M. E. Berens, A. F. Shamji, P. A. Clemons, B. R. Stockwell, S. L. Schreiber, Dependency of a therapy-resistant state of cancer cells on a lipid peroxidase pathway. *Nature* **547**, 453–457 (2017).

48. S. Marino, M. Vooijs, H. van Der Gulden, J. Jonkers, A. Berns, Induction of medulloblastomas in p53-null mutant mice by somatic inactivation of Rb in the external granular layer cells of the cerebellum. *Genes Dev.* **14**, 994–1004 (2000).

49. Y. Zhang, S. Xiong, B. Liu, V. Pant, F. Celii, G. Chau, A. C. Elizondo-Fraire, P. Yang, M. J. You, A. K. el-Naggar, N. E. Navin, G. Lozano, Somatic Trp53 mutations differentially drive breast cancer and evolution of metastases. *Nat. Commun.* **9**, (2018).

50. R. J. Platt, S. Chen, Y. Zhou, M. J. Yim, L. Swiech, H. R. Kempton, J. E. Dahlman, O. Parnas, T. M. Eisenhaure, M. Jovanovic, D. B. Graham, S. Jhunjhunwala, M. Heidenreich, R. J. Xavier, R. Langer, D. G. Anderson, N. Hacohen, A. Regev, G. Feng, P. A. Sharp, F. Zhang, CRISPR-Cas9 knockin mice for genome editing and cancer modeling. *Cell* **159**, 440–455 (2014).

51. W. Xue, S. Chen, H. Yin, T. Tammela, T. Papagiannakopoulos, N. S. Joshi, W. Cai, G. Yang, R. Bronson, D. G. Crowley, F. Zhang, D. G. Anderson, P. A. Sharp, T. Jacks, CRISPR-mediated direct mutation of cancer genes in the mouse liver. *Nature* **514**, 380–+ (2014).

52. S. M. Moyer, A. R. Wasylishen, Y. Qi, N. Fowlkes, X. Su, G. Lozano, p53 drives a transcriptional program that elicits a non-cell-autonomous response and alters cell state in vivo. *Proc. Natl. Acad. Sci. U.S.A.* **117**, 23663–23673 (2020).

53. S. L. Wolock, R. Lopez, A. M. Klein, Scrublet: Computational identification of cell doublets in single-cell transcriptomic data. *Cell Syst.* **8**, 281–291.e9 (2019).

54. I. Korsunsky, N. Millard, J. Fan, K. Slowikowski, F. Zhang, K. Wei, Y. Baglaenko, M. Brenner, P. R. Loh, S. Raychaudhuri, Fast, sensitive and accurate integration of single-cell data with Harmony. *Nat. Methods* **16**, 1289–1296 (2019).

55. T. Stuart, A. Butler, P. Hoffman, C. Hafemeister, E. Papalexi, W. M. Mauck III, Y. Hao, M. Stoeckius, P. Smibert, R. Satija, Comprehensive integration of single-cell data. *Cell* **177**, 1888–1902.e21 (2019).

56. E. Becht, L. M. Innes, J. Healy, C.-A. Dutertre, I. W. H. Kwok, L. G. Ng, F. Ginhoux, E. W. Newell, Dimensionality reduction for visualizing single-cell data using UMAP. *Nat. Biotechnol.* **37**, 38–44 (2019).

57. T. L. Bailey, M. Boden, F. A. Buske, M. Frith, C. E. Grant, L. Clementi, J. Ren, W. W. Li, W. S. Noble, MEME SUITE: Tools for motif discovery and searching. *Nucleic Acids Res.* **37**, W202–W208 (2009).

58. A. Dobin, C. A. Davis, F. Schlesinger, J. Drenkow, C. Zaleski, S. Jha, P. Batut, M. Chaisson, T. R. Gingeras, STAR: Ultrafast universal RNA-seq aligner. *Bioinformatics* **29**, 15–21 (2013).

59. M. I. Love, W. Huber, S. Anders, Moderated estimation of fold change and dispersion for RNA-seq data with DESeq2. *Genome Biol.* **15**, 550 (2014).

60. Z. Tang, B. Kang, C. Li, T. Chen, Z. Zhang, GEPIA2: An enhanced web server for large-scale expression profiling and interactive analysis. *Nucleic Acids Res.* **47**, W556–W560 (2019).